


## RESEARCH ARTICLE

# A moist-thermal quasi-geostrophic model for monsoon depressions

A. K. Chaudhri<sup>1,2</sup>  | M. P. Byrne<sup>1</sup>  | R. K. Scott<sup>2</sup> <sup>1</sup>School of Earth and Environmental Sciences, University of St Andrews, St Andrews, UK<sup>2</sup>School of Mathematics and Statistics, University of St Andrews, St Andrews, UK**Correspondence**

A. K. Chaudhri, School of GeoSciences, University of Edinburgh, Edinburgh, EH9 3FF, UK.

Email: [achaudh2@ed.ac.uk](mailto:achaudh2@ed.ac.uk)**Present address**

A. K. Chaudhri, School of GeoSciences, The University of Edinburgh, Edinburgh, UK

**Funding information**

St Leonard's College Interdisciplinary Doctoral Scholarship awarded by the University of St Andrews

**Abstract**

Monsoon depressions (MDs) are synoptic-scale storms that occur during the summer phase of the global monsoon cycle and whose dynamical mechanisms remain incompletely understood. To gain insight into the dynamics governing the large-scale structure of MDs, we formulate an idealised moist-thermal quasi-geostrophic model that includes distinct thermal and moisture fields in simple forms. A linear-stability analysis of the model, with basic states corresponding to typical monsoon conditions, shows three distinct mode classifications: thermal-Rossby modes, heavy precipitating modes, and a moist-thermal mode. In the linearised model, the presence of a background precipitation gradient strengthens thermal-Rossby modes by coupling the dynamics to latent heating. The separation of heavy precipitating modes from fast-propagating thermal-Rossby modes is further examined with numerical experiments of large-amplitude MDs. Wind-induced evaporation is found to amplify large-amplitude MDs in conditions analogous to those over the northern Bay of Bengal. An energetic analysis shows the pathways by which the MDs derive energy from the background state. A further series of experiments through a continuum of meridional temperature gradients demonstrates the sensitivity of large-scale MD dynamics to the background state and suggests a possible mechanism to explain variations in the propagation direction of MDs.

**KEYWORDS**

idealised modelling, moist-thermal quasi-geostrophic dynamics, monsoon depressions

## 1 | INTRODUCTION

The term “monsoon depression” (MD) is used to refer to a broad class of synoptic-scale, low-pressure systems that form and propagate during the summer phase of the monsoon cycle (Hunt et al., 2016; Shukla, 1977). MDs are frequently observed in the Indian Ocean, West Pacific, and across the global monsoon, and contribute a large fraction of summertime precipitation in those regions (Hurley & Boos, 2015). Whether in response to a warming climate

or natural variability (Cohen & Boos, 2014; Vishnu et al., 2018, 2020), changes in MDs—such as in their precipitation intensity and genesis frequency (Kitoh et al., 2013; Krishnamurti et al., 2013; Rastogi et al., 2018)—present significant societal challenges in monsoon regions. As such, it is important to build fundamental understanding of the dynamics of MDs and their response to evolving background conditions.

MDs are particularly prevalent in the south Asian monsoon region and importantly deliver substantial

summer rainfall over a region of habitation and food production for a large proportion of the global population (Hurley & Boos, 2015). Whether South Asian MDs spontaneously form in situ Lindzen et al. (1983) or are seeded by westward-propagating disturbances originating from West Pacific tropical storms (Krishnamurti et al., 1977), it is understood that MDs intensify in the moist, convectively unstable air over the Bay of Bengal (Adames & Ming, 2018b; Clark et al., 2020; Cohen & Boos, 2016; Diaz & Boos, 2019a, 2019b) at a latitude of approximately 20°N (Hurley & Boos, 2015; Krishnamurti et al., 1977). MDs in this region develop in the tropical–subtropical boundary, a warm, moist region, with non-negligible Coriolis forces and significant meridional temperature gradients (Zhang & Fueglistaler, 2020), before propagating westnorthwestward over the South Asian continent (Chen et al., 2005; Krishnamurti et al., 1977; Lindzen et al., 1983). MDs have a typical outer diameter of 2000 km and deliver a precipitation maximum of approximately 20 mm·day<sup>-1</sup> across an area of roughly 1000 km in diameter (Hunt et al., 2016; Hurley & Boos, 2015). As an example, Figure 1 shows a Hovmöller diagram along 20°N and a snapshot of a 2006 MD. The disturbance propagated westward with phase speed 5–6°W/day—corresponding with Krishnamurti et al. (1977)—amplified into an MD over the warm surface waters of the Bay of Bengal and made landfall over South Asia during the following days at a slower propagation speed—consistent with Boos et al. (2015).

Summer conditions over the northern Bay of Bengal are baroclinic, with vertical wind shear and tropospheric temperatures that typically increase with latitude (Krishnamurti et al., 2013; Shukla, 1977). It is well observed that MDs deliver precipitation westsouthwest of their centre (Chen et al., 2005; Hurley & Boos, 2015; Rao & Rajamani, 1970) and that both the horizontal and vertical structures of thermal and moist-convective processes are significant in shaping the dynamics of MDs (Clark et al., 2020; Diaz & Boos, 2019a; Krishnakumar et al., 1992; Krishnamurti et al., 2013).

Early models have shown success in capturing key characteristics of MDs. In particular, numerical experiments have shown how MD propagation can be modelled by moisture convergence driving a mass overturning that in turn generates vorticity westnorthwest of the vortex centre (Goswami, 1987). Additionally, models have shown how amplification of small-amplitude disturbances by barotropic instability can organise rainfall on length scales comparable to MDs (Lindzen et al., 1983). More recently, single-layer shallow-water models have been used to understand the role of different barotropic growth mechanisms in quasi-linear waves and large-amplitude MD-like disturbances (Adames & Ming, 2018a; Suhas &

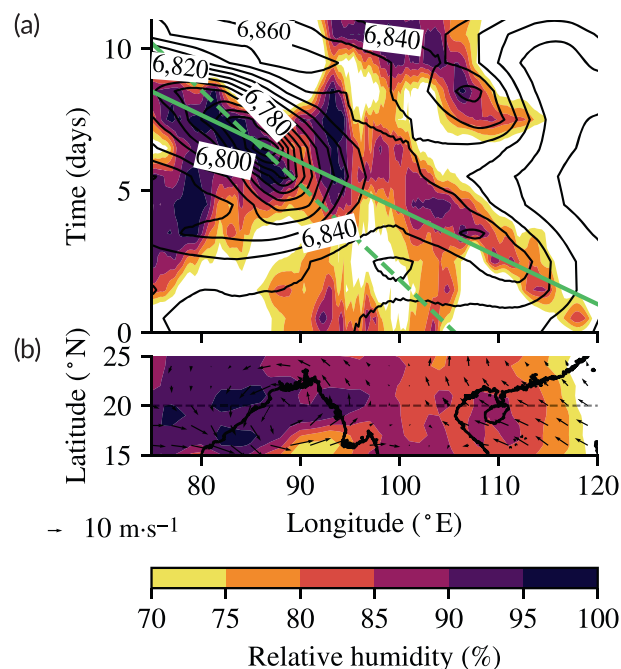


**FIGURE 1** (a) Hovmöller diagram along 20°N beginning on June 25, 2006, showing hourly European Centre for Medium-Range Weather Forecasts Reanalysis v5 (Hersbach et al., 2020) relative humidity at 500 hPa (shading) and 500 hPa geopotential height (labelled contours); (b) July 1, 2006, daily-mean 500 hPa wind vectors (quivers) and relative humidity (shading) showing a depression over the northern Bay of Bengal. Green lines have been added to (a) to indicate 6°W/day (solid), which is a typical phase speed for a tropical disturbance propagating and amplifying into a depression from Krishnamurti et al. (1977); and 3°W/day (dashed), which represents the upper end of the revised 2–3 m·s<sup>-1</sup> westward propagation speed for Bay of Bengal monsoon depressions from Boos et al. (2015). [Colour figure can be viewed at [wileyonlinelibrary.com](http://wileyonlinelibrary.com)]

Boos, 2023). Adames and Ming (2018a) used a linearised framework to demonstrate intensification of monsoonal low-pressure systems by moisture–vortex instability under the condition of similarly westward-propagating dry-Rossby and moist modes. By varying meridional wind shear and moisture gradients, Suhas and Boos (2023) demonstrated a barotropic growth of vortex circulation depending on positive meridional wind shear, and an organisation of precipitation west of MD-like perturbations under positive meridional moisture gradients. We expand upon previous investigations into MDs using idealised modelling by introducing an energetic analysis to gain insight into the role of evaporative feedbacks in MD amplification. Additionally, we investigate the sensitivity of MD-like disturbances to the background temperature gradient. This experiment provides a mechanism for the inhibition of MDs during winter conditions as well as an insight into propagation changes under different climate conditions.

Using a multilayered model, Krishnakumar et al. (1992) found westward-propagating modes with a wavelength of approximately 2500 km, reminiscent of MDs, and further found that ageostrophic effects were needed to explain the development of features consistent with observations. More recently, Diaz and Boos (2019b) demonstrated a mechanism for barotropic energy transfer from a meridional and vertically sheared background state that couples latent heating into a dry Rossby-like mode to generate growth. They also showed that wind-induced surface heat exchange provides a mechanism for additional MD growth (Diaz & Boos, 2019b). Though Cohen and Boos (2016) have ruled out baroclinic instabilities as the growth mechanism for Bay of Bengal MDs, moist-baroclinic models have been shown to capture key aspects of MDs (Clark et al., 2020; Diaz & Boos, 2019a, 2019b). Additional motivation to explore the mechanics of MD-like disturbances in a solely barotropic model follows from the results of Adames (2021), who demonstrated the importance of moist-vortex instability versus baroclinic instability in MD growth.

To avoid some of the complexity inherent in multi-layer models and aid physical interpretation of the results, we consider here the idealised set-up of a single-layer, moist-thermal, quasi-geostrophic model. Though simple, our model succeeds in reproducing some of the key features of MDs (e.g., propagation direction and speed) and retains the nonlinear effects of horizontal advection and wind-dependent evaporation, along with the feedback between dynamics and diabatic heating. In this idealised approach, we combine linear stability analysis with numerical experiments to investigate MD-like variability in a simple framework. As well as providing information about the free modes of the system, the linear analysis also provides (by comparison with the fully nonlinear equations) information about the importance of nonlinear interactions for the development of MDs. Our study focuses on several questions: How effectively can a single-layer quasi-geostrophic model support MD-like dynamics? By classifying modes, can Rossby-like waves provide insights into MD dynamics? And in such a model, what is the importance of background conditions in determining the dynamics of large-scale MD-like perturbations?

The remainder of the paper is organised as follows. In Section 2, we outline the derivation of our model from the shallow-water equations. In Section 3, the magnitudes of the moist-thermodynamic parameters in the model are assigned based on a series of simple arguments relating the idealised equations to tropical tropospheric time-scales. In Section 4, we conduct a linear stability analysis of the model, and in Section 5 we examine numerical experiments using the fully nonlinear equations. In Section 6,

the sensitivities of the model dynamics to a range of linear background states are explored, before we conclude in Section 7 with a discussion.

## 2 | A MOIST-THERMAL QUASI-GEOSTROPHIC MODEL

### 2.1 | Quasi-geostrophic equations

Our model is based on a simplification of the moist, thermal shallow-water equations derived by Zerroukat and Allen (2015) and is related to the thermal quasi-geostrophic model of Warnford and Dellar (2013), except that we also include idealised moist processes, using explicit temperature and specific humidity fields. Similar shallow-water models incorporating the effects of moisture have been studied in other contexts by Zhao et al. (2021) and Kurganov et al. (2021). As already discussed herein, our aim is to obtain a model that retains the dominant dynamical and physical processes, including nonlinear advection and the moist-thermal interactions of evaporation, condensation, and latent heat release. We simplify the shallow-water model of Zerroukat and Allen (2015) further by making the quasi-geostrophic approximation for low Rossby-number flows. We also simplify the moist processes by letting condensation equal precipitation and instantaneously removing condensed water from the system, thus ignoring details of cloud physics and re-evaporation of falling precipitation. We do, however, allow for the possibility that surface fluxes depend on surface wind speed by using a simple model of wind-induced evaporation.

The moist, thermal shallow-water equations can be written, following Zerroukat and Allen (2015), as

$$\frac{D}{Dt}u - fv + gh_x = S^x, \quad (1a)$$

$$\frac{D}{Dt}v + fu + gh_y = S^y, \quad (1b)$$

$$\frac{D}{Dt}h + h(\nabla \cdot \mathbf{u}) = 0, \quad (1c)$$

$$\frac{D}{Dt}\theta = LP - R, \quad (1d)$$

$$\frac{D}{Dt}r = E - P, \quad (1e)$$

$$S^a = g\left(\theta h_a + \frac{1}{2}h\theta_a\right), \quad a \in \{x, y\}, \quad (1f)$$

where derivatives are denoted by subscripts. Here,  $(u, v)$  is the horizontal velocity vector,  $h = H + h'$  is the layer thickness with average thickness  $H$  and a perturbation  $h'/H \ll 1$ ,  $\theta$  is a dimensionless temperature perturbation, and  $r$  is a dimensionless specific humidity. One difference between this model and the formulation of the thermal

quasi-geostrophic model in Warnford and Dellar (2013) is that the thermal field here represents a perturbation about an arbitrary reference temperature, with  $\theta \ll 1$ , rather than a buoyancy field. Other variables on the left-hand sides are standard; in particular,  $f$  is the Coriolis parameter, and  $g$  is the acceleration due to gravity.

The terms on the right-hand sides of Equations (1a)–(1f) represent various sources and sinks:  $S^x$  and  $S^y$  are the zonal and meridional momentum sources due to the interaction of pressure and temperature gradients, an approximation of the buoyancy source term from the primitive equations;  $E$  is the moisture source due to surface evaporation;  $P$  is the moisture sink due to precipitation;  $LP$  is the temperature source due to latent heat release, where  $L$  is the latent heat of vaporisation; and  $R$  is a temperature relaxation term. The forms for  $E$ ,  $P$ , and  $R$  are defined in Section 3.

We provide, next, an informal derivation of our quasi-geostrophic approximation; a rigorous derivation via asymptotic expansion can be found in Warnford and Dellar (2013) for the dry equations in terms of a buoyancy or reduced gravity variable in place of our temperature perturbation. Kurganov et al. (2020) also derive the equations in terms of buoyancy.

First, the balance equation (Charney, 1955) is recovered from the leading order terms of the divergence of the momentum equations, Equations (1a) and (1b), after neglecting  $D/Dt$  terms. Using  $h'/H \ll 1$  and  $\theta \ll 1$ , this reduces to

$$-f_0 \hat{\mathbf{k}} \cdot \nabla \times \mathbf{u} + g \nabla^2 h = \frac{1}{2} g H \nabla^2 \theta. \quad (2)$$

As in Charney (1955), we introduce a quasi-geostrophic streamfunction  $\psi$ , with  $(u, v) = (-\psi_y, \psi_x)$ , that satisfies

$$gh' = f_0 \psi + \frac{1}{2} g H \theta. \quad (3)$$

Next, we retain the dominant terms in the Taylor expansion for the full shallow-water potential vorticity (PV),

$$Q \equiv \frac{f + \nabla^2 \psi}{H + h'} \approx \frac{1}{H} \left( f + \nabla^2 \psi - \frac{f_0}{H} h' \right), \quad (4)$$

to obtain the quasi-geostrophic PV in our model:

$$q = f + (\nabla^2 - L_D^{-2}) \psi - \frac{1}{2} f_0 \theta, \quad (5)$$

where  $L_D = \sqrt{gH}/f_0$  is the deformation radius. Note that the difference in sign in the last term from the equivalent expressions in Warnford and Dellar (2013) and Kurganov et al. (2020) results from the use of temperature in place of buoyancy, which are related via  $b = g(1 - \theta)$ .

The two formulations are identical, and since our focus is on the atmosphere we follow the notation of Zerroukat and Allen (2015).

An evolution equation for  $q$  is obtained by taking the curl of Equations (1a) and (1b):

$$\begin{aligned} \frac{D}{Dt} (f + \zeta) - (\nabla \cdot \mathbf{u})(f + \zeta) &= S_x^y - S_x^x \\ &= -\frac{1}{2} g (h_x \theta_y - h_y \theta_x), \end{aligned} \quad (6)$$

where  $\zeta = \nabla^2 \psi$  is the relative vorticity. Using Equation (1c) to eliminate  $\nabla \cdot \mathbf{u}$  and using Equation (3) to write  $h'$  in terms of  $\psi$  and  $\theta$ , we then obtain to leading order

$$\frac{D}{Dt} (f + \zeta - L_D^{-2} \psi - \frac{1}{2} f_0 \theta) = -\frac{1}{2} f_0 (\psi_x \theta_y - \psi_y \theta_x). \quad (7)$$

The full equations of our model are therefore

$$\frac{D}{Dt} q = -\frac{1}{2} f_0 \mathbf{u} \cdot \nabla \theta, \quad (8a)$$

$$\frac{D}{Dt} \theta = LP - R, \quad (8b)$$

$$\frac{D}{Dt} r = E - P. \quad (8c)$$

## 2.2 | Moist-thermal formulations

We now derive expressions for the moist-thermal functions  $E$ ,  $P$ , and  $R$  based on simple moist-thermodynamic considerations. A key quantity that will be used in their definition is the saturation mixing ratio  $r_{\text{sat}}$  that determines the amount of water vapour a parcel of air at a given temperature can hold. At the simplest level of approximation we take  $r_{\text{sat}}$  to vary linearly with  $\theta$ , a simplification of the exponential fit given by Zerroukat and Allen (2015) (eq. A.9) that holds to a reasonable extent over the relatively narrow range of temperatures considered here.

Absorbing the constant of proportionality into our (arbitrary) scaling for temperature, we have simply

$$r_{\text{sat}} = \theta. \quad (9)$$

Note that we have chosen not to include separate fields for liquid water and water vapour. Separate fields, as used in Zerroukat and Allen (2015) and Rostami and Zeitlin (2022), would allow excess humidity to be condensed to a liquid phase forming clouds, which feedback on the dynamics via both latent heating and radiative effects. In the spirit of creating a minimal model, however, we choose to limit the number of dynamical variables and sources of nonlinearity and retain a single water field.



For simplicity, we let precipitation take the form of a relaxation on excess moisture,  $r - r_{\text{sat}} = r - \theta$ , with

$$P = \gamma(r - \theta)\mathcal{H}(r - \theta), \quad (10)$$

where  $\gamma$  is a constant modulating the precipitation rate and  $\mathcal{H}$  is the Heaviside step function. The evaporation term  $E$  is defined by a prescribed spatial function,  $S^E(x, y)$ , which may be interpreted as a moisture availability term that can be modulated by a wind-dependent coefficient to simulate wind-induced evaporation. We also prescribe an equilibrium temperature profile,  $\theta^e = \theta^e(x, y)$ , and let  $R$  take the form of a Newtonian relaxation toward  $\theta^e$ :

$$R = \nu(\theta - \theta^e), \quad (11)$$

where  $\nu$  is the dry relaxation rate.

In Section 3, we use a series of simple arguments to determine how the strengths of the moist-thermal processes may be associated with typical tropical time-scales.

### 3 | MODEL PARAMETERS

#### 3.1 | Equilibrium states

We first consider simple steady-state equilibria,  $\bar{\theta}$  and  $\bar{r}$ , of the system in Equations (8a)–(8c) with  $u = v = 0$ . The corresponding steady-state PV is  $\bar{q} = \beta y - \frac{1}{2}f_0\bar{\theta}$ . Equilibria correspond to balances between sources and sinks in the thermal and specific humidity equations, given respectively by

$$R = LP \quad \text{and} \quad P = E. \quad (12)$$

Recall here that both  $E$  and  $\theta^e$  are prescribed forcing functions, with  $E$  possibly also depending on wind speed as described earlier herein. We consider first the case of non-zero  $E$ . Because of the Heaviside in Equation (10), nonzero  $E$  cannot be balanced in the steady-state unless  $\bar{r} \geq \bar{\theta}$ , in which case the atmosphere is supersaturated everywhere and always precipitating. In this case, Equation (12) may be solved to give

$$\bar{\theta} = \frac{LE}{\nu} + \theta^e, \quad (13)$$

$$\bar{r} = \frac{LE}{\nu} + \theta^e + E/\gamma. \quad (14)$$

A second case may be considered in which  $E = 0$  everywhere. In this case,  $\bar{r} \leq \bar{\theta}$ ,  $P = 0$ , and the balance is given simply by  $R = 0$ ; that is,

$$\bar{\theta} = \theta^e.$$

Simple forms for  $E$  and  $\theta^e$  are obtained by considering typical summer and winter conditions over the Bay of

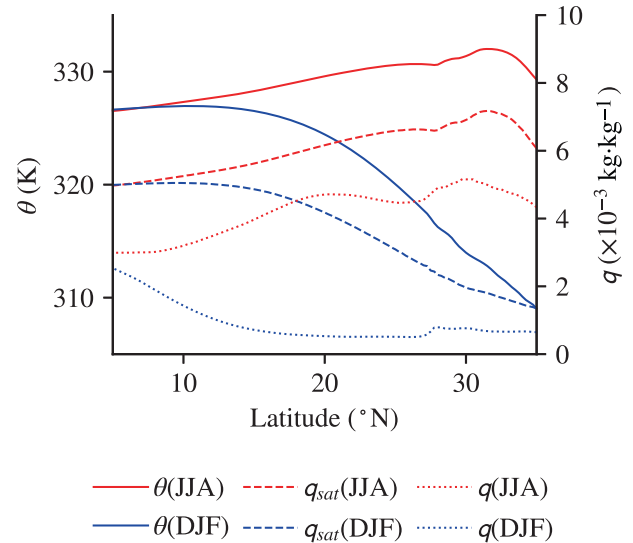


**FIGURE 2** Zonally averaged (75–95°E) meridional profiles of December–February (DJF; blue) and June–August (JJA; red) potential temperature (solid), saturation specific humidity (dashed), and specific humidity (dotted) at 500 hPa. All data are from European Centre for Medium-Range Weather Forecasts Reanalysis v5 and have been averaged from 2000 to 2019. [Colour figure can be viewed at [wileyonlinelibrary.com](http://wileyonlinelibrary.com)]

Bengal and adjacent continent, in the region 75–95°E. Meridional profiles of June–August and December–February potential temperature, specific humidity, and saturation specific humidity at 500h Pa are shown in Figure 2. Around 20°N the specific humidity and potential temperature depend approximately linearly on latitude outside the tropical troposphere where weak temperature gradients generally prevail (Sobel & Bretherton, 2000). Suhas and Boos (2023) demonstrated growth in a two-dimensional shallow-water model by barotropic instability on a background state with meridional wind shear, and Adames and Ming (2018a) found moisture–vortex instability on a background with a meridional specific humidity gradient, both inspired by conditions over the Bay of Bengal and South Asia. Here, in contrast, we choose to focus on the role of meridional temperature gradients (rather than humidity gradients) in the growth of MD-like disturbances. Additionally, we analyse the role of a precipitation gradient in a linearised version of our model.

We therefore take our basic state to satisfy

$$\bar{\theta}_y = \alpha, \quad (15)$$

$$\bar{r}_y = 0, \quad (16)$$

where  $\alpha$  is a constant—small and positive in summer, larger and negative in winter—implying a background precipitation gradient  $\bar{P}_y = -\gamma\alpha$ . This choice then imposes

a constraint on the possible forcing functions,  $E$  and  $\theta^e$ . From Equation (13) it follows that we must have, for the case  $E \neq 0$ , and without mean-state wind-induced evaporation,

$$E_y = -\alpha\gamma, \quad (17)$$

$$\theta_y^e = \alpha \left( \frac{\gamma L}{\nu} + 1 \right). \quad (18)$$

In the non-precipitating case with  $E = 0$  and  $\bar{r} \leq \bar{\theta}$ , we have simply

$$\theta_y^e = \alpha.$$

Note that the corresponding steady-state PV gradient is  $\bar{q}_y = \beta + \frac{1}{2}f_0\bar{\theta}_y$ . Thus, the difference between summer and winter equilibrium temperature states can be expected to lead to a difference in the Rossby wave propagation speeds. As shown later, however, nonlinearity plays an important role in modifying this simple dependence.

### 3.2 | Moist-thermal time-scales

To set the moist thermal parameters— $\nu$ ,  $\gamma$ , and  $L$ —we consider the moist-thermal equations in the absence of advection:

$$\theta_t = L\gamma(r - \theta)\mathcal{H}(r - \theta) - \nu(\theta - \theta^e), \quad (19a)$$

$$r_t = E - \gamma(r - \theta)\mathcal{H}(r - \theta). \quad (19b)$$

For a state  $r = \bar{r} + r'$ ,  $\theta = \bar{\theta} + \theta'$ , where  $r \geq \theta$ , we have

$$\theta'_t = L\gamma(r' - \theta') - \nu\theta', \quad (20)$$

$$r'_t = -\gamma(r' - \theta'), \quad (21)$$

which can be used to infer values for  $\nu$ ,  $\gamma$ , and  $L$  so that relaxation rates correspond to typical tropical time-scales. As suggested by Cronin and Emanuel (2013), there are three distinct time-scales in the tropical troposphere: a dry radiative cooling time-scale at fixed specific humidity,  $\tau_{\text{dry}}$ , relevant when  $r < \theta$ ; a moist radiative cooling time-scale at fixed relative humidity,  $\tau_{\text{moist}} = 100$  days, relevant when  $r > \theta$  and substantially longer than  $\tau_{\text{dry}}$  as a given temperature change is associated with a substantially larger moist enthalpy change compared with the fixed-specific humidity case; and a much shorter precipitation time-scale,  $\tau_{\text{precip}}$ , based on convective relaxation.

From Equation (20), we identify  $\nu^{-1}$  with  $\tau_{\text{dry}}$ , which we take equal to 20 days, which is comparable to the time-scale of radiative cooling from Tompkins and Craig (1998). Subtracting Equation (21) from Equation (20) and neglecting the slower dry radiative time-scale term gives

$$(\theta' - r')_t = -\gamma(L + 1)(\theta' - r'). \quad (22)$$

We therefore identify  $[\gamma(L + 1)]^{-1}$  with  $\tau_{\text{precip}}$ , which we take here to be 0.25 days, chosen so as to represent the fast process of relaxation of excess water and convective precipitation. Finally, adding Equation (20) and  $L$  times Equation (21), and using the constraint that  $\theta' - r'$  relaxes to zero on a much shorter time-scale than either  $\tau_{\text{dry}}$  or  $\tau_{\text{moist}}$ , gives

$$(1 + L)\theta'_t = -\nu\theta', \quad (23)$$

from which we identify  $(1 + L)/\nu$  with  $\tau_{\text{moist}}$ , taken here to be 100 days.

We thus obtain the parameter values

$$\nu = \frac{1}{20} \text{ day}^{-1}; \quad \gamma = \frac{4}{5} \text{ day}^{-1}; \quad L = 4.$$

### 3.3 | Wind-induced evaporation

We also define a bulk evaporation term as the product of a prescribed evaporation rate  $S^E$ , and a term that depends on wind speed (e.g., Penman & Keen, 1948),

$$E = S^E \sqrt{c_{\text{WI}}^2 \mathbf{u}^2 + G}, \quad (24)$$

where  $G$  is a gust term allowing for water to be evaporated at zero wind speed. To compare with observations, we will consider  $G = 1$ , but in simulations where wind-induced evaporation is included, to avoid domain-wide precipitating basic states, we specify a gust term of zero ( $G = 0$ ).

The parameter  $c_{\text{WI}}$  is used to scale the strength of wind-induced evaporation. To estimate an approximate magnitude for  $c_{\text{WI}}$ , we consider the average precipitation rates during the summer monsoon season,  $\bar{P}$ , and during an active MD,  $P_{\text{MD}}$ . Assuming  $S^E$  equals the summer mean precipitation in the monsoon region (i.e., taking  $E = S^E$  and neglecting convergence of water vapour into the region by the winds),

$$\bar{P} = S^E, \quad (25)$$

and during an MD (again neglecting convergence of water vapour),

$$P_{\text{MD}} = S^E \sqrt{c_{\text{WI}}^2 u_{\text{MD}}^2 + 1}, \quad (26)$$

where  $u_{\text{MD}}$  is a characteristic wind speed. Therefore,

$$c_{\text{WI}} = \frac{1}{u_{\text{MD}}} \sqrt{\frac{P_{\text{MD}}^2}{\bar{P}^2} - 1}. \quad (27)$$

We use precipitation data from the European Centre for Medium-Range Weather Forecasts Reanalysis v5 Hersbach et al. (2020) (Figure 3) to estimate a lower

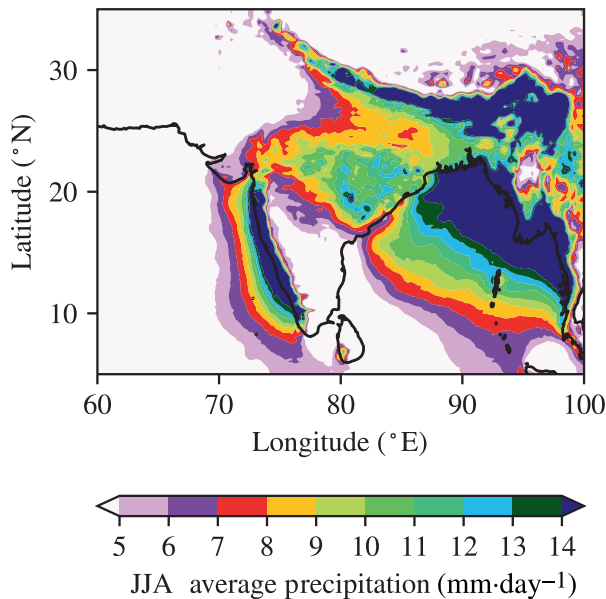


**FIGURE 3** Climatological June–August (JJA) precipitation (2000–2019) over South Asia from European Centre for Medium-Range Weather Forecasts Reanalysis v5. During the summer monsoon season there is heavy rainfall along the Western Ghats and eastern Bay of Bengal. The Gangeatic Plain, of interest for the study of monsoon depressions, receives an average precipitation of 5–11 mm·day<sup>-1</sup> during JJA. [Colour figure can be viewed at [wileyonlinelibrary.com](http://wileyonlinelibrary.com)]

bound on  $c_{WI}$ . We take  $\bar{P} = 8 \text{ mm}\cdot\text{day}^{-1}$  as a typical June–August seasonal-average precipitation rate that will also include precipitation delivered by MDs. We also take  $u_{MD} = 1000 \text{ km}\cdot\text{day}^{-1} \approx 12 \text{ m}\cdot\text{s}^{-1}$  as a characteristic maximum wind speed in MDs Hurley and Boos (2015); Hunt et al. (2016) and  $P_{MD} = 20 \text{ mm}\cdot\text{day}^{-1}$  as a typical MD precipitation rate Hurley and Boos (2015). From these values, we calculate a lower bound on  $c_{WI}$  of

$$c_{WI} = 2.3 \text{ days} / 1000 \text{ km}. \quad (28)$$

### 3.4 | Scaling of the dynamical and temperature fields

We take the background Coriolis parameter  $f_0 = 2\Omega \sin 20^\circ\text{N}$ , where  $\Omega = 2\pi/\text{day}$ . The gradient  $\beta$  is defined by  $\beta = df/a \, d\phi$  evaluated at  $\phi = \phi_0$ , where  $a$  is the planetary radius. The northward distance from  $\phi_0$  is  $y = a(\phi - \phi_0)$ . The only other parameter of dynamical importance is the deformation radius  $L_D$ , which we take to be 1000 km. For ease of the numerical implementation, and in the results presented herein, we scale all lengths in terms of  $L_D$ .

Following Zerroukat and Allen (2015), we define our dimensionless temperature by  $\theta = T/300 \text{ K}$ . Figure 2 shows potential temperature gradients near  $20^\circ\text{N}$  of

$\mathcal{O}(10/1000 \text{ km})$ , corresponding to a dimensionless  $\theta_y$  of  $\mathcal{O}(0.03)$ . To explore the dependence of the dynamics on background gradients more generally, we consider  $\theta_y^e$  in the extended range  $[-0.5, 0.5]$ .

## 4 | LINEAR ANALYSIS

We conduct a linear analysis of the model equations to determine stable and unstable modes and how these modes may contribute to the genesis of a larger amplitude anomaly. First, we linearise the formulations of precipitation and evaporation to

$$P = \gamma(r - \theta), \quad (29a)$$

$$E = S^E, \quad (29b)$$

where the Heaviside function and the dependence of  $E$  on wind speed have been dropped, and  $\theta^e$  and  $S^E$  are linear functions of  $x, y$ . As a result of Equation (29a), any change in temperature  $\theta$  also changes specific humidity  $r$ , and the linearised model experiences a non-physical “reverse precipitation” moisture source for  $\theta > r$ .

We expand the model equations for a small perturbation  $\mathbf{A}' = (\psi', \theta', r')$  from a background state,  $\bar{\mathbf{A}} = (\bar{\psi}, \bar{\theta}, \bar{r})$ , that is a function of  $y$  only. The background meridional velocity is  $V = \bar{\psi}_x = 0$ , and we define the background zonal velocity as  $U = -\bar{\psi}_y$ . The basic state must satisfy

$$L\gamma(\bar{r} - \bar{\theta}) - v(\bar{\theta} - \theta^e) = 0, \quad (30a)$$

$$S^E - \gamma(\bar{r} - \bar{\theta}) = 0, \quad (30b)$$

which can be solved to give

$$\bar{\theta} = v^{-1}LS^E + \theta^e, \quad (31a)$$

$$\bar{r} = (\gamma^{-1} + v^{-1}L)S^E + \theta^e. \quad (31b)$$

The equations for the perturbation fields are then

$$(\nabla^2 - L_D^{-2})\psi'_t = -\beta\psi'_x + \frac{f_0}{2}\theta'_t, \quad (32a)$$

$$\theta'_t = -U\theta'_x - \bar{\theta}_y\psi'_x + L\gamma(r' - \theta') - v\theta', \quad (32b)$$

$$r'_t = -Ur'_x - \bar{r}_y\psi'_x - \gamma(r' - \theta'), \quad (32c)$$

and by posing wave solutions of the form  $\psi' = \tilde{\psi} e^{i(k_x x + k_y y - \omega t)}$ , and so on, these reduce to the algebraic system

$$-(k_x^2 + k_y^2 + L_D^{-2})\omega\tilde{\psi} = \left(\beta + \frac{f_0\bar{\theta}_y}{2}\right)k_x\tilde{\psi} + \frac{f_0}{2}[Uk_x - i(\gamma L + v)]\tilde{\theta} + i\frac{f_0}{2}\gamma L\tilde{r}, \quad (33a)$$

$$\omega\tilde{\theta} = \bar{\theta}_y k_x \tilde{\psi} + [Uk_x - i(\gamma L + v)]\tilde{\theta} + i\gamma L\tilde{r}, \quad (33b)$$

$$\omega\tilde{r} = \bar{r}_y k_x \tilde{\psi} + i\gamma\tilde{\theta} + [Uk_x - i\gamma]\tilde{r}. \quad (33c)$$

A similar linearisation, but without the distinct temperature field, was considered by Monteiro and Sukhatme (2016).

At this point it is helpful to introduce the shorthand notation  $\tilde{\beta} = \beta + \frac{1}{2}f_0\bar{\theta}_y$  and  $\kappa^2 = k_x^2 + k_y^2 + L_D^{-2}$ . Equations (33a)–(33c) can then be written in terms of  $\omega$ , giving the matrix equation

$$\omega \begin{pmatrix} \tilde{\psi} \\ \tilde{\theta} \\ \tilde{r} \end{pmatrix} = M \begin{pmatrix} \tilde{\psi} \\ \tilde{\theta} \\ \tilde{r} \end{pmatrix}, \quad (34)$$

where

$$M = \begin{bmatrix} -\frac{\tilde{\beta}k_x}{\kappa^2} & \frac{f_0}{2} \frac{-Uk_x + i(\gamma L + \nu)}{\kappa^2} & \frac{f_0}{2} \frac{-iyL}{\kappa^2} \\ \bar{\theta}_y k_x & Uk_x - i(\gamma L + \nu) & iyL \\ \bar{r}_y k_x & i\gamma & Uk_x - iy \end{bmatrix}. \quad (35)$$

Solving  $\det M = 0$  gives three eigenvalues  $\omega$ ; that is, the dispersion relation between frequency and wave number for each free mode of the system. The eigenvalues may be complex and modes with  $\text{Im}(\omega) > 0$  are unstable, growing modes, which will eventually dominate the dynamics. The zonal phase speed of each mode is  $u_{\text{phase}} = \text{Re}(\omega)/k_x$ . The complex frequency  $\omega$  depends on the background state through  $\bar{\theta}_y$  and  $\bar{r}_y$ . For cases where  $\bar{\theta}_y = \bar{r}_y = 0$  the moist-thermodynamics are decoupled from PV and the dispersion relation simplifies to that for dry Rossby waves:

$$\omega_{\text{Rossby}} = -\frac{\beta k_x}{k_x^2 + k_y^2 + L_D^{-2}}. \quad (36)$$

We further categorise the linear modes according to their moist-thermal structure by considering the

eigenvector associated with each eigenvalue. Normalising with respect to  $\tilde{\psi}$ , the eigenvectors may be written

$$\begin{pmatrix} \tilde{\psi} \\ \tilde{\theta} \\ \tilde{r} \end{pmatrix} = \begin{pmatrix} 1 \\ A_\theta e^{i\phi_\theta} \\ A_r e^{i\phi_r} \end{pmatrix}, \quad (37)$$

where  $A_\theta$  and  $A_r$  are real amplitudes of the thermal and moisture fields relative to the streamfunction field, and  $\phi_\theta$  and  $\phi_r$  are real phase differences between the thermal and moisture fields and the streamfunction field. The associated precipitation is

$$\tilde{P} = \tilde{r} - \tilde{\theta} = A_P e^{i\phi_P}, \quad (38)$$

where  $A_P$  and  $\phi_P$  can be expressed in terms of  $A_\theta$ ,  $A_r$ ,  $\phi_\theta$ , and  $\phi_r$ .

Physically, the phase relationship between  $\tilde{\psi}_i$  and  $\tilde{P}_i$  indicates where precipitation maxima occur relative to streamfunction maxima:  $\phi_P = \pi$  corresponds to fields out of phase, where a precipitation maximum is located at a minimum of  $\psi$ , or a locally cyclonic vorticity anomaly;  $\phi = \pi/2$  corresponds to precipitation maxima located between cyclonic and anticyclonic anomalies, where the flow in the  $y$  direction is strongest.

Figure 4 shows the eigenvalue and eigenvector dependence on  $k_x$  for non-precipitating background states with a positive meridional temperature gradient (summer conditions). Linear modes are either neutrally stable or decaying. A thermal-Rossby wave (mode-1) has zero precipitation but does depend on background gradients through  $\tilde{\beta}$ , with faster westward propagation under more positive meridional temperature gradients. The precipitating modes (modes-2 and -3) are stationary. The strongest

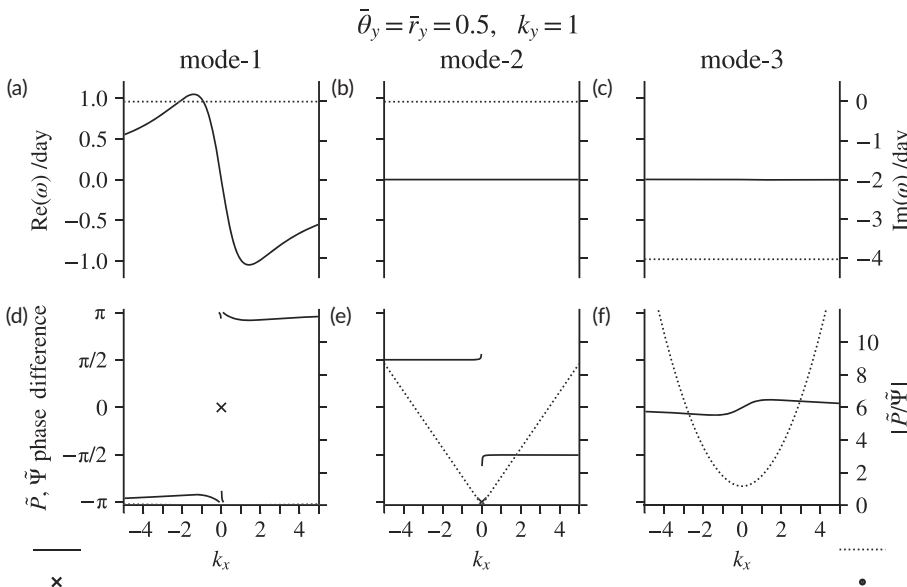
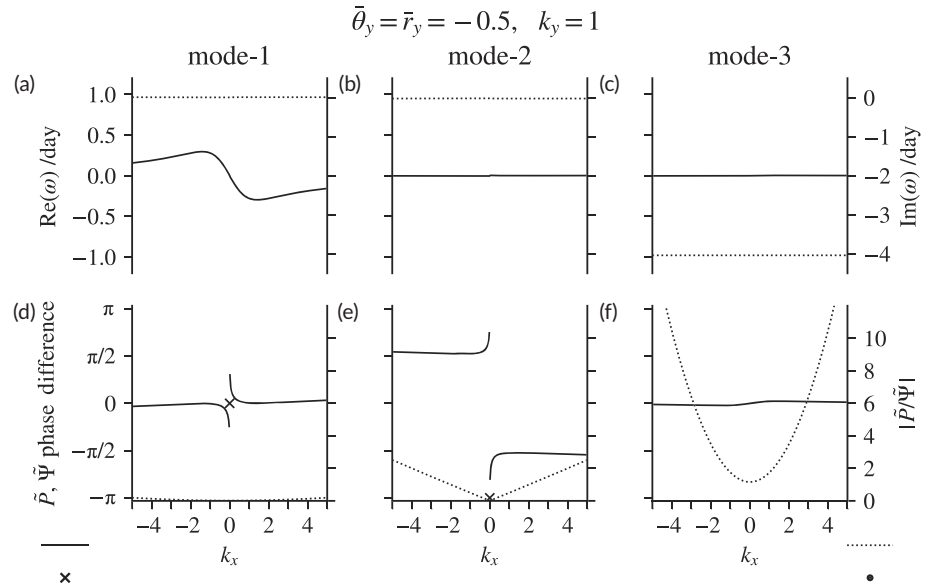


**FIGURE 4** Eigenvalue and precipitation component of eigenvector solutions under background conditions of positive meridional temperature gradient and relative humidity,  $k_y = 1/1000$  km,  $L_D = 1000$  km, for  $k_x \in [-5, 5]$ . Solutions are organised by eigenvalue–eigenvector pairs sorted for  $-\text{Im}(\omega)$  by column: mode-1 (a, d), mode-2 (b, e), and mode-3 (c, f). Solid (dotted) lines are used for solutions plotted against the left-hand (right-hand) axes, with singular solutions indicated by a cross (dot). In this case the thermal-Rossby mode (mode-1) does not organise precipitation.



**FIGURE 5** As Figure 4, except for background conditions with a negative meridional temperature gradient.



precipitating mode (mode-3) decays rapidly, with a precipitation rate that increases with wave number. An additional neutrally stable mode (mode-2) has precipitation maxima located between streamfunction maxima and minima ( $\phi_P \approx \pi/2$ ) and the precipitation strength increases linearly with  $k_x$ . None of these modes show a dependence of the growth rate on the wave number, and so the linear dynamics does not indicate any mechanism for scale selection. The corresponding case of negative temperature gradient is shown in Figure 5. Though there are some quantitative changes the qualitative pattern is similar.

Further insight into the relationship between flow and precipitation perturbations can be obtained by neglecting radiative cooling, which acts on longer time-scales than both precipitation and advection in typical MD-like flows.

By defining the precipitation anomaly

$$P' = \gamma(r' - \theta'), \quad (39)$$

we can combine Equations (32c) and (32b) into a single equation for  $P'$ , and  $\theta'_t$  in Equation (32a) can be eliminated by Equation (32b). For the special case of no background flow,  $U = 0$ , this results in the coupled system in the two fields  $\psi'$  and  $P'$ :

$$(\nabla^2 - L_D^{-2})\psi'_t = -\tilde{\beta}\psi'_x + \frac{f_0}{2}LP', \quad (40)$$

$$P'_t = -\bar{P}_y\psi'_x - \gamma(L+1)P'. \quad (41)$$

Proceeding with a wave solution as before then leads to the matrix problem

$$\omega \begin{pmatrix} \tilde{\psi} \\ \tilde{P} \end{pmatrix} = \begin{bmatrix} -\frac{\tilde{\beta}k_x}{\kappa^2} & -i\frac{f_0}{2}\frac{L}{\kappa^2} \\ \bar{P}_yk_x & -i\gamma(L+1) \end{bmatrix} \begin{pmatrix} \tilde{\psi} \\ \tilde{P} \end{pmatrix}. \quad (42)$$

When  $\bar{P}_y = 0$ , the eigenvalue problem gives two distinct linear modes. The first is a thermal-Rossby mode, with dispersion relation  $\omega = \omega_R = -\tilde{\beta}k_x/\kappa^2$  as before, for which the eigenvector has  $\tilde{P} = 0$ . The second mode is a non-propagating precipitating mode with  $\omega = \omega_P = -i\gamma(L+1)$  that decays as excess humidity is relaxed out of the system. The eigenvector for this second mode has

$$\frac{\tilde{P}}{\tilde{\psi}} = \frac{\kappa^2\gamma(L+1) + i\tilde{\beta}k_x}{f_0L/2}. \quad (43)$$

Figure 6 shows the dependence of  $\omega$  and mode structure on the background temperature gradient for the case  $\bar{P}_y = 0$ . The Rossby wave mode propagates west at a speed dependent on  $\bar{\theta}_y$ , through  $\tilde{\beta}$  as before. The other, precipitating, mode is stationary, with amplitude and phase that depend only weakly on  $\bar{\theta}_y$ , being dominated by the term involving  $\kappa^2$ . The decay time for the precipitating mode is  $1/[\gamma(L+1)]$ . This mode is essentially the same precipitating mode as the stronger of the two precipitating cases described earlier (mode-3 in Figures 4c,f and 5c,f).

To find  $\omega$  when  $\bar{P}_y \neq 0$ , we can rewrite Equation (44) in the form

$$\omega \begin{pmatrix} \tilde{\psi} \\ \tilde{P} \end{pmatrix} = \begin{bmatrix} \omega_R & -i\frac{f_0}{2}\frac{L}{\kappa^2} \\ \bar{P}_yk_x & \omega_P \end{bmatrix} \begin{pmatrix} \tilde{\psi} \\ \tilde{P} \end{pmatrix}, \quad (44)$$

where  $\omega_R$  and  $\omega_P$  are the two eigenvalues obtained when  $\bar{P}_y = 0$ . The eigenvalues are given by the roots of

$$\omega^2 - (\omega_R + \omega_P)\omega + \omega_R\omega_P + i\frac{f_0}{2}\frac{L\bar{P}_yk_x}{\kappa^2} = 0. \quad (45)$$

Adames and Ming (2018a) have previously found a dispersion relation that similarly describes dry Rossby

$$\bar{P}_y = 0, k_x = k_y = 1$$

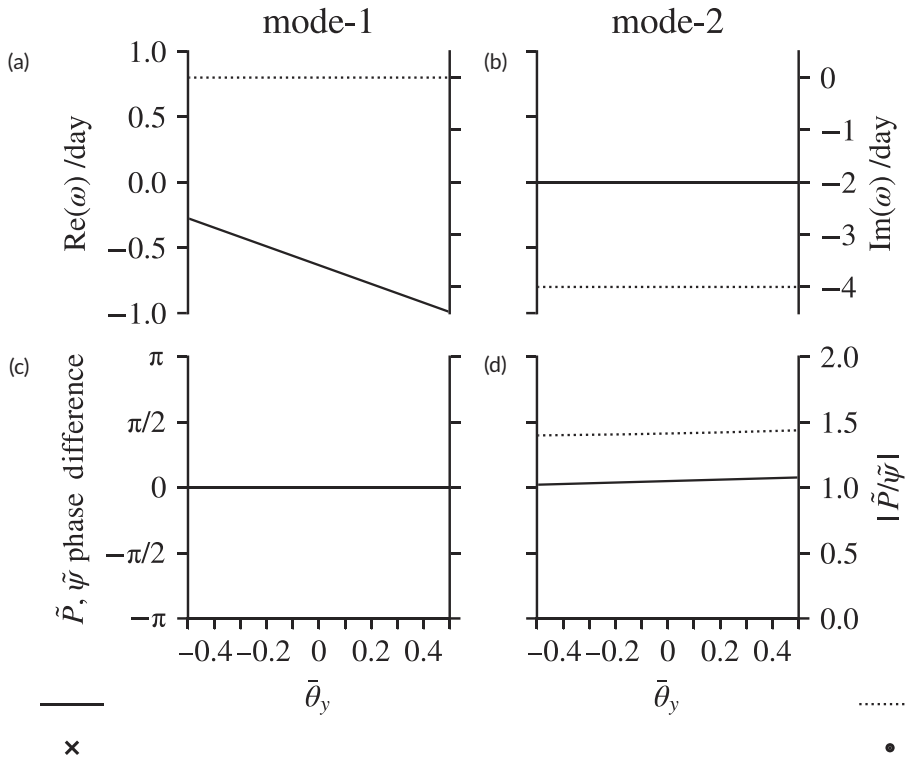


**FIGURE 6** Eigenvalues (a, b) and eigenvectors (c, d) for the thermal-Rossby (mode-1) and precipitating (mode-2) solutions of Equation (44) for fixed wave number and  $\bar{P}_y = 0$ .

$$\bar{\theta}_y = 0, k_x = k_y = 1$$

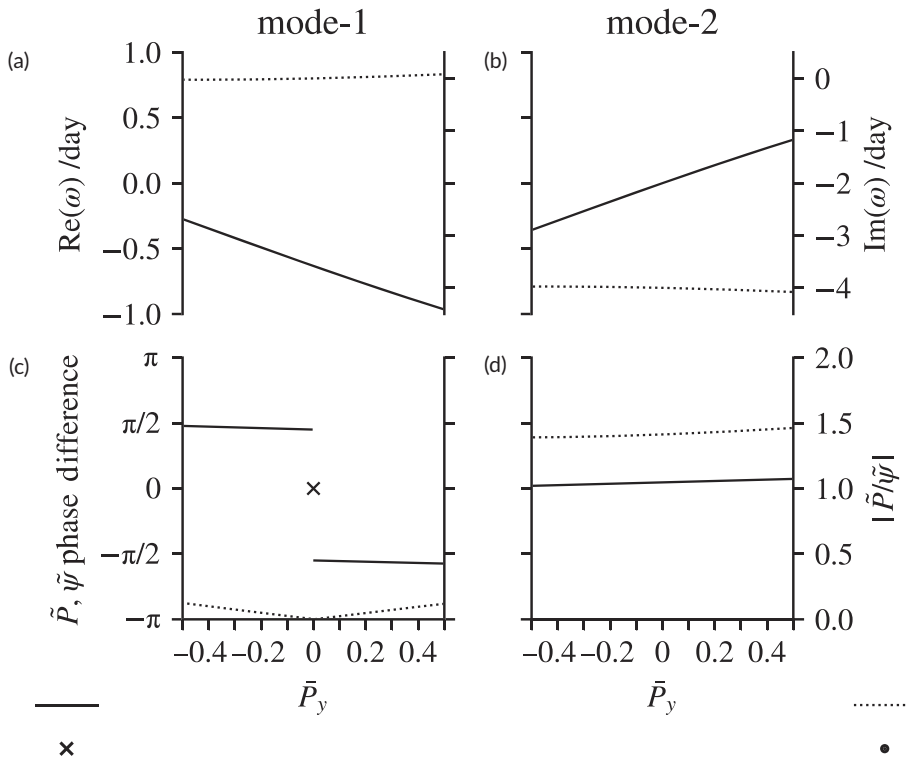


**FIGURE 7** Eigenvalues (a, b), and eigenvectors (c, d), for the thermal-Rossby (mode-1) and precipitating (mode-2) solutions of Equation (44) for fixed wave number and  $\bar{\theta}_y = 0$ .

modes and precipitating modes, and which couples moisture–vortex instability to monsoonal disturbances in an idealised model. Here, we specifically identify the role

of a background precipitation gradient in coupling moist and dry-thermal dynamics in the linearised version of our model. As  $\bar{P}_y$  is varied, the solutions of Equation (45)

vary from the decoupled Rossby-like and precipitating modes to modes with dispersion relations that combine  $\omega_R$  and  $\omega_P$ . Additionally, the wave number enters the imaginary part of the dispersion relation, suggesting a possible scale selection by instability. This can be seen in Figure 7, which shows the dependence of eigenvalues and eigenvectors on background precipitation gradient for the case  $\theta_y = 0$ .

The phase difference implies that the Rossby-like mode organises precipitation where the flow is down the background precipitation gradient. The Rossby-like mode amplifies for all  $\bar{P}_y$ , drawing energy from the latent heating associated with precipitation. The dipole of positive to negative  $P'$  across a propagating positive vorticity anomaly acts as a dipole of diabatic energy transfer. From the time-derivative of Equation (5), this couples vorticity generation west (and dissipation east) of the anomaly, aiding the westward propagation. When  $\bar{P}_y > 0$  the modes propagate in opposite directions. There is a range of negative  $\bar{P}_y$  where both modes have  $\text{Re}(\omega) < 0$ , implying westward propagation of both modes.

## 5 | NUMERICAL RESULTS

We next explore the fully nonlinear dynamics of the model by solving the model equations numerically. Following a brief outline of the numerical method (Section 5.1), we first consider (in Section 5.2) the extent to which small-amplitude disturbances are described by the linear analysis carried out in Section 4, then nonlinear precipitation with the Heaviside dependence in Equation (10) is reinstated. We then (in Section 5.3) illustrate the behaviour of finite-amplitude disturbances and the effects of nonlinear advection. Finally (in Section 5.4), we consider the energy transfers within the system that sustain the growth of perturbations.

### 5.1 | Numerical implementation

The model equations (Equations 8a–8c) were time-integrated in a periodic channel of size  $12L_D \times 6L_D$  (with  $L_D = 1000$  km; see Section 3.4), with a free slip boundary condition at the channel walls ( $y = 0, 6$ ). The large spatial domain is chosen to reduce the influence of the lateral and periodic boundary conditions. The numerical method used is a standard pseudo-spectral method, in which the Fourier modes are integrated forward in time using a fourth-order Runge–Kutta scheme, whereas the nonlinear terms are calculated in physical space. The spectral modes are fully dealiased by truncating with a two-thirds rule. A weak, scale-selective hyperdiffusion of the form  $\nabla^4$  is included on all prognostic fields for

numerical stability, preventing the build up of enstrophy and moisture/temperature variance at the smallest scales, while having practically no effect on the large-scale dynamics. A grid of  $256 \times 128$  points was found to be sufficient to resolve the relatively large-scale flow features of interest.

### 5.2 | Comparison with linear stability analysis

To compare the numerical experiments with the linear analysis, we use the same background temperature and moisture gradients, setting  $\theta_y^e = 0.5$  (summer-like) or  $\theta_y^e = -0.5$  (winter-like), and then initialise the model with  $\bar{\theta}_y = \bar{r}_y = \theta_y^e$ . To this background state we then introduce a perturbation via the PV. When single  $(k_x, k_y)$  modes are perturbed the resulting wave motions follow closely the predictions of the linear analysis.

To illustrate more general evolution, we consider perturbations comprising a range of wave numbers and define the initial perturbation PV to be

$$q'(x, y) = a \sin\left(\frac{\pi y}{3}\right) \sum_{n=1}^{20} \cos\left(nx + \frac{10\pi}{p_n}\right), \quad (46)$$

where  $p_n$  are the first 20 prime numbers used for phase shifting so as not to incidentally overrepresent lower wave numbers, and  $a$  is a small amplitude set to  $a = 0.01$  for comparison with the linear stability analysis.

Figure 8a shows a Hovmöller plot for a small-amplitude perturbation on a background temperature gradient of  $\theta_y^e = 0.5$  along the line  $y = 1.5$ , where the perturbation is initially largest. Though the perturbations remain small in amplitude, so that the nonlinear advection term remains negligible, nonlinearity is nonetheless present in the precipitation field. These examples support the predictions from the linear stability analysis. There are low-wave-number Rossby modes with fast westward propagation, whereas stationary precipitation anomalies grow rapidly across a range of scales in the  $x$ -direction set by the initial perturbation. As in Figure 4, the faster propagating, neutrally stable, thermal-Rossby modes are decoupled from a set of near-stationary strongly precipitating modes. Figure 8b shows the same initial perturbation but with  $\theta_y^e = -0.5$ . The non-precipitating Rossby wave modes propagate more slowly since negative  $\bar{\theta}_y$  reduces the effective  $\bar{\beta}$ . At this latitude there is a fast drain of moisture due to precipitation triggered by flow down the background specific humidity gradient, where the perturbed fields have  $r - \theta > 0$ . This results in flow up the background specific humidity gradient where  $r - \theta < 0$ ; in the linearised

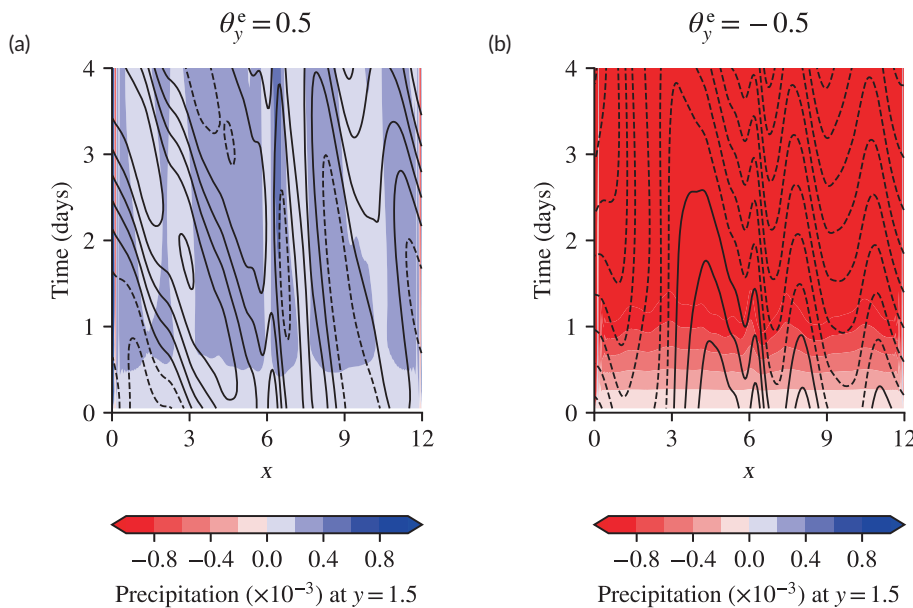


**FIGURE 8** Hovmöller plots of small-amplitude perturbations on temperature gradients of (a)  $\theta_y^e = 0.5$  and (b)  $\theta_y^e = -0.5$  at  $y = \pi/4$  in domain coordinates. The background gradient in (a) supports westward-propagating linear waves that are decayed in (b). The growth of stationary precipitating modes is evident in (b). Contours show the streamfunction, and colours indicate the precipitation rate. [Colour figure can be viewed at [wileyonlinelibrary.com](http://wileyonlinelibrary.com)]

equations this humidity deficit would be a moisture source. There are slower propagating non-precipitating modes on this winter-like background state, as suggested by the thermal-Rossby wave dispersion relation:

$$\omega = -\frac{\tilde{\beta}k_x}{\kappa^2}. \quad (47)$$

On a background of constant relative humidity, with a specific humidity gradient, the moist-thermal fields in regions of precipitation will relax to  $RH = 1$  ( $r = \theta$ ) through loss of specific humidity (reduction in  $r$ ). The Heaviside term in the precipitation equation introduces nonlinearity into the moisture and temperature equations.

For linear background moisture and temperature fields, precipitation may be triggered when flow is directed down a specific humidity ( $\bar{r}$ ) gradient:  $r$  is conserved following the flow, whereas  $\theta$  relaxes towards a lower value of  $\theta^e$ , resulting in  $r > \theta$ , triggering precipitation. Owing to latent heat release the  $\theta$  relaxation rate is subdued on the longer moist time-scale  $\tau_{\text{moist}}$ , compared with the faster time-scale  $\tau_{\text{dry}}$ . The reduction in time-scales due to latent heat release leads to a weaker temperature gradient in precipitating regions than would occur in non-precipitating regions, where the final  $\theta$  is closer to  $\theta^e$ .

The results of linear-stability analysis and these experiments with small-amplitude perturbations show a decoupling between stationary but amplifying precipitation and “dry linear Rossby modes” that, in our range of parameter space, have westward propagation favoured by  $\theta_y^e > 0$ . From these results, we are motivated to conduct numerical experiments for large-amplitude disturbances to examine moist-thermal effects on the dynamics where an MD-like perturbation is sufficiently strong that the nonlinear

advection of the moisture and temperature fields organising evaporation and precipitation are leading terms.

### 5.3 | MD-like perturbations

We next consider the evolution of a larger amplitude disturbance, which we base loosely on the composite MD structures constructed by Hunt et al. (2016). Specifically, we define a PV anomaly comprising a Gaussian vortex of the form

$$q_v = \frac{U_{\text{max}} e^{1/2}}{R_{\text{max}}} (2 + R_{\text{max}}^2 L_D^{-2}) e^{-(x^2+y^2)/(2 \times 0.11^2)}, \quad (48)$$

where  $R_{\text{max}}$  and  $U_{\text{max}}$  are suitable constants chosen to produce the desired structure of the initial perturbation. Here, we take  $R_{\text{max}} = 0.5$  and  $U_{\text{max}} = 1$ , corresponding in dimensional units of approximately 500 km and 12 m·s<sup>-1</sup> respectively. The actual maximum velocity of the vortex is close, though not exactly equal, to  $U_{\text{max}}$ , and the vortex is similar to the approximate Gaussian structure of the composite MD constructed by Hunt et al. (2016). The radial decay of the Gaussian is sufficiently rapid that the perturbation PV near the domain edges is weak, although during the time evolution propagation of the disturbance will eventually bring it closer to the boundaries, with possible interaction effects. The key independent constants used in the formulation of the full model are summarised in Table 1.

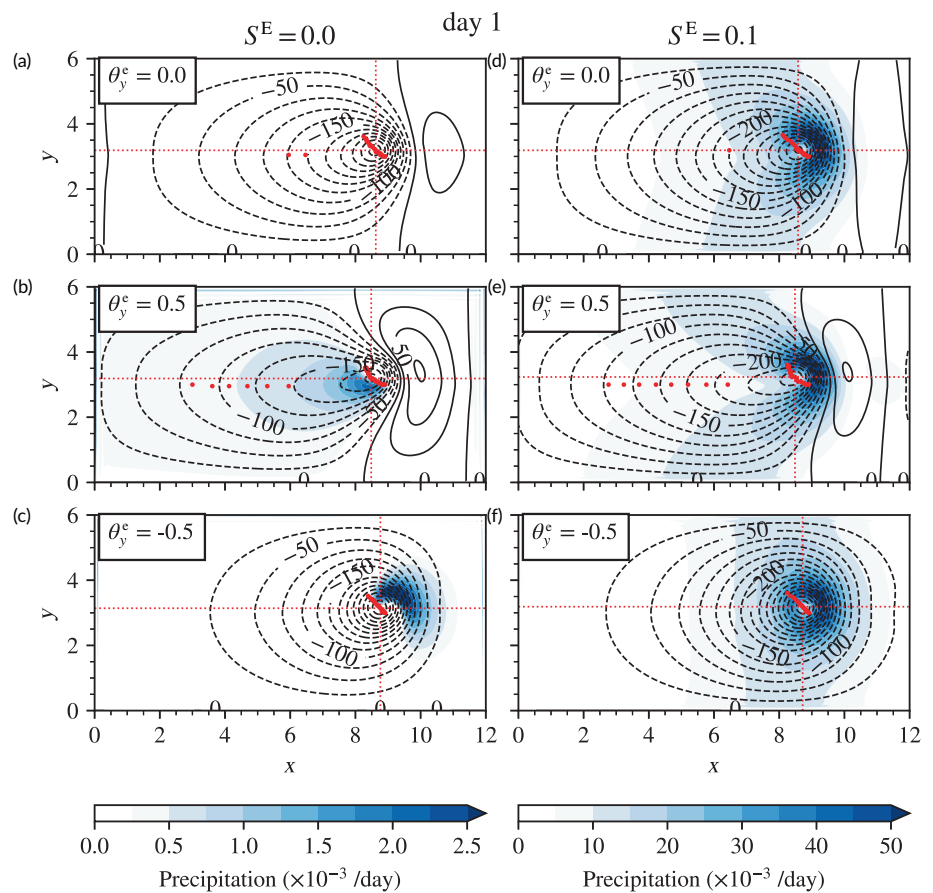
The experiments using this perturbation are firmly in the nonlinear regime (Figure 9), and the wind speeds associated with the perturbation are on the order of  $\mathcal{O}(L_D \text{days}^{-1})$ . Although the maximum Rossby number for



**TABLE 1** Summary of key independent constants used in the full model.

| Constant   | Description   |
|--|---|
| $f_0 = 4.3 \text{ day}^{-1}$                       | Coriolis parameter at $20^\circ\text{N}$  |
| $\beta = 1.9/1000 \text{ km}\cdot\text{day}^{-1}$  | Meridional gradient of $f$ at $20^\circ\text{N}$  |
| $L_D = 1000 \text{ km}$                            | Rossby radius of deformation  |
| $\tau_{\text{moist}} = 100 \text{ days}$           | Time-scale of radiative cooling at a constant relative humidity                             |
| $\tau_{\text{dry}} = 20 \text{ days}$              | Time-scale of radiative cooling at a constant specific humidity                             |
| $\tau_{\text{precip}} = 0.25 \text{ days}$         | Time-scale of relaxation of excess humidity as precipitation                                |
| $S^E \in \{0, 0.1\} \text{ day}^{-1}$              | Potential evaporation rate  |
| $c_{\text{WI}} = 2.3 \text{ days}/1000 \text{ km}$ | Coefficient scaling wind-induced evaporation  |
| $U_{\text{max}} = 12 \text{ m}\cdot\text{s}^{-1}$  | Approximate maximum wind speed of initialised prototype monsoon depression                  |
| $R_{\text{max}} = 500 \text{ km}$                  | Radius from vortex centre to highest wind speed of initialised prototype monsoon depression |

**FIGURE 9** Snapshots after 1 day of experiments with Gaussian perturbations on background conditions with relative humidity of 1 and  $\theta_y^e = 0$  (a, d),  $\theta_y^e = 0.5$  (b, e), and  $\theta_y^e = -0.5$  (c, f). Panels (a)–(c) omit wind-induced evaporation, and panels (d)–(f) include wind-induced evaporation (with  $S^E = 0.1$ ). The streamfunction  $\psi$  (black contours) is plotted in intervals of  $25 \times 10^3 \text{ km}^2 \cdot \text{day}^{-1}$ , with labels in units of  $10^3 \text{ km}^2 \cdot \text{day}^{-1}$ . The precipitation rate is shown with shading. Note the different precipitation colour scales for experiments without and with wind-induced evaporation. Red dots track minima in the streamfunction over 2 days in intervals of 0.1 days, and red cross-hairs indicate local streamfunction minima in each snapshot. [Colour figure can be viewed at [wileyonlinelibrary.com](http://wileyonlinelibrary.com)]



the flow approaches 0.5, we expect the quasi-geostrophic model to remain a reasonable approximation to the full dynamics for much of the evolution. Background thermal gradients vary as  $\nabla\bar{\theta} \sim \mathcal{O}(L_D^{-1})$ , so to a first approximation we expect the magnitude of the advective term in the PV equation, Equation (8a), to scale as

$$\left| \frac{D}{Dt} q \right| \sim \frac{f_0}{2} U_{\text{max}} \nabla\bar{\theta} \approx 1 \text{ day}^{-2}. \quad (49)$$

Advection by the Gaussian anomaly also leads to changes in the moist-thermal background states on a time-scale

$$\tau_{\text{adv}} \sim \frac{R_{\text{max}}}{U_{\text{max}}} = 0.5 \text{ days}, \quad (50)$$

which is 40 times shorter than  $\tau_{\text{dry}}$ . There can also be a significant change to the moisture source term due to wind-induced evaporation since  $c_{\text{WI}} U_{\text{max}} S^E \approx 2.3 S^E$ .

Figure 9 shows snapshots of streamfunction and precipitation after 1 day for a series of experiments with different background conditions. The experiments have  $\theta_y^e = 0.0, 0.5, -0.5$ , with each background gradient run with and without wind-induced evaporation. In the experiment with  $\theta_y^e = 0$  and no wind-induced evaporation (Figure 9a), there is no interaction between the dynamics and the moisture or temperature fields, so this run effectively isolates the nonlinear dynamics due to the advection of PVy. Low-amplitude domain-scale modes propagate westward away from the large-amplitude depression core. This propagation follows the Rossby wave equation, Equation (36), with faster westward propagation at smaller wave numbers. After approximately 2 days, a local streamfunction minimum becomes separated from the core and propagates westward with phase speed of around  $2 \text{ day}^{-1}$ . However, the large-amplitude perturbation at the core propagates northwestward by beta-drift due to the advection and wrapping of the background vorticity gradient by the substantial wind speeds of the vortex (Lam & Dritschel, 2001; Mohebalhojeh & Dritschel, 2001). Indeed, adiabatic beta-drift has been identified as a propagation mechanism for MDs by Boos et al. (2015). Here, by varying the background conditions, we illustrate how this mechanism can be modulated by the various moist-thermal effects.

Including wind-induced evaporation, with  $\theta_y^e = 0$ , couples precipitation to the wind speed. Initially, this forms a band of precipitation, and raised temperatures, following the radially symmetric winds around the core; but as longer modes radiate faster westward, contours of streamfunction gather on the eastern flank of the depression and separate on the western flank (Figure 9d). Therefore, precipitation intensifies on the eastern flank and extends in lobes north and south of the depression core. Though the propagation path is similar to the case without wind-induced evaporation (cf. Figure 9a), the perturbation deepens with this precipitation and draws energy from latent heating following Equation (8a), which can be written in the form

$$\frac{D}{Dt}(\nabla^2 - L_D^{-2})\psi = -\beta v + \frac{1}{2}f_0\theta_t, \quad (51)$$

showing that a monotonically increasing  $\theta$  field leads to increases in  $q$ , and hence decreases in the streamfunction.

The nonlinear dynamics are further modulated by the inclusion of a background temperature gradient. For  $\theta_y^e = 0.5$ , the low-amplitude domain-scale modes propagate faster (Figure 9b,e), consistent with the higher effective  $\tilde{\beta}$  in the dispersion relations derived in Section 4. The propagation of the depression core is westnorthwestward over the first day, but tracks northnorthwestward over the second day (red dots in Figure 9b). This is attributed to

distortion of the initial disturbance and interference due to periodicity of the domain and interaction with propagating domain-scale modes.

With background temperature gradients, but still without wind-induced evaporation (e.g., Figure 9b), precipitation is triggered by advection of specific humidity that condenses as it flows down  $\theta^e$  gradients. This precipitation is organised in a lobe extending out of the southwestern quadrant, with maximum amplitude of approximately  $2 \times 10^{-3} \text{ day}^{-1}$  after the first day of the experiment. Though precipitation is generated in this model without moisture convergence or convection, precipitation organised in the southwestern quadrant is reminiscent of that observed in MDs in the Bay of Bengal (Hunt et al., 2016; Hurley & Boos, 2015). Higher temperatures induced by this precipitation may contribute to westward propagation in a manner similar to the moist vortex instability described in Adames and Ming (2018a). With wind-induced evaporation (Figure 9e), precipitation is again organised with the faster wind speeds on the eastern flank of the depression core. This occurs as thermal-Rossby modes with lower wave number propagate westward faster than those with higher wave number, causing a sharper gradient in streamfunction on the eastern flank of the vortex. The resulting wind-induced evaporation contributes to precipitation rates that are an order of magnitude greater than those without wind-induced evaporation for this choice of  $S^E$  and  $c_{WI}$ .

In contrast, on a background gradient of  $\theta_y^e = -0.5$  (Figure 9c), the propagation of thermal-Rossby waves is slowed and there is little radiation of large-scale modes away from the depression core. This helps maintain a coherent perturbation. Without wind-induced evaporation, precipitation is organised on the eastern flank of the disturbance, still down specific humidity gradients. This coherence means that, when including wind-induced evaporation (Figure 9f), the disturbance shows the strongest amplification on this particular background gradient.

Despite the importance of nonlinear dynamics where the perturbation is strongest, these cases reveal certain dynamical similarities to the small-amplitude experiments. Like in the earlier Hovmöller diagrams for small-amplitude perturbations (see Figure 8), Figure 10 shows that for the large-amplitude perturbation with a background gradient of  $\theta_y^e = 0.5$  there are fast-propagating domain-scale linear-like thermal-Rossby waves that radiate from the depression core, whereas the mode with heavy precipitation propagates more slowly westward, organised at a smaller scale by stronger wind speeds. The vortex interaction with temperature gradients drives faster westward-propagating dry waves, with the precipitating core propagating westward at around  $500 \text{ km} \cdot \text{day}^{-1}$ .

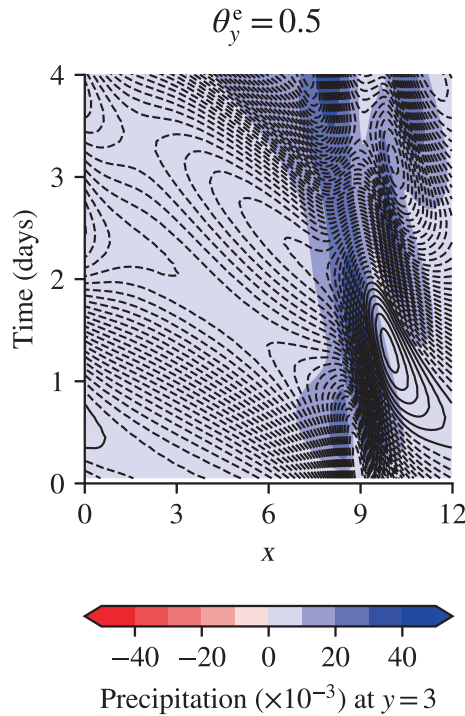


**FIGURE 10** Hovmöller plot of a large-amplitude perturbation on a background state with  $\theta_y^e = 0.5$ . Contours indicate the streamfunction and colours show the precipitation rate. [Colour figure can be viewed at [wileyonlinelibrary.com](http://wileyonlinelibrary.com)]

Notwithstanding these similarities to the linear dynamics, nonlinear effects are significant, especially local to the strong-amplitude vortex centre. On a flat background temperature,  $\theta_y^e = 0$ , without wind-induced evaporation (Figure 9a), the vortex produced by the initial Gaussian perturbation suffers strong attenuation as fast-westward-propagating ( $\approx 3000 \text{ km} \cdot \text{day}^{-1}$ ), domain-scale (12,000 km) Rossby-waves radiate from a slower propagating, smaller diameter core of fast winds. This core propagates northwestward with nonlinear beta-drift. A background temperature gradient reduces the northward component of propagation and enhances the westward component, and a negative background gradient prevents westward propagation altogether. This sensitivity to the background condition is discussed in results across a continuum of  $\theta_y^e$  in Section 6.

## 5.4 | Energetic analysis

The role of wind-induced evaporation in influencing MD-like perturbations can be further examined in terms of the zonal-mean energy budget. Energy in the system can reside in the form of kinetic energy, available potential energy (related to streamfunction, or layer thickness in the parent shallow-water model), and moist-thermal enthalpy. Figure 11 shows the leading

terms in the energy budget for an integration of the Gaussian anomaly with  $\theta_y^e = 0.5$ . Zonal-mean kinetic energy,  $\frac{1}{2} \langle |\nabla \psi|^2 \rangle_x$ , is greatest either side of the initial perturbation (Figure 11a). The presence of the vortex flattens local temperature gradients in the zonal mean. In this configuration, reduced temperatures north of the vortex act as an energy source of diabatic heating from radiative disequilibrium, whereas enhanced temperatures lose energy south of the vortex centre. This diabatic transfer contributes to higher wind speeds north of the depression centre. The inclusion of wind-induced evaporation couples evaporation to higher wind speeds, enhancing the diabatic transfer of energy to the flow and creating a positive feedback between heating and the flow.

Available potential energy (see Figure 11b) is defined as

$$\Delta\theta(\Delta h)^2 = \Delta\theta(1 + \Delta\theta + f_0^{-1}L_D^{-2}\psi)^2, \quad (52)$$

where  $\Delta\theta = \theta - \theta^e$ . Contributions to  $\Delta\theta$  include both adiabatic effects associated with the advection of the background  $\theta$  by the flow (Figure 11d) and the diabatic effects of latent heating (Figure 11c) and radiative relaxation. These effects are concentrated in the centre of the vortex anomaly.

It is also instructive to consider the transfer of enstrophy between different components of the flow. Potential enstrophy integrated over the domain is defined as

$$\mathcal{Z} = \int \int_{\text{domain}} \left( q + \frac{f_0}{2}\theta \right)^2 dx dy, \quad (53)$$

and the rate of change in time can be written

$$\mathcal{Z}_t = \int \int_{\text{domain}} 2 \left( q + \frac{f_0}{2}\theta \right) \frac{\partial}{\partial t} \left( q + \frac{f_0}{2}\theta \right) dx dy, \quad (54a)$$

$$= f_0 \int \int_{\text{domain}} \left( q + \frac{f_0}{2}\theta \right) (-\nabla\theta \cdot \mathbf{u} + LP - R) dx dy, \quad (54b)$$

$$= \mathcal{Z}_t^{\text{Adv}} + \mathcal{Z}_t^{\text{Precip}} + \mathcal{Z}_t^{\text{Rad}}, \quad (54c)$$

where  $-\mathbf{u} \cdot \nabla\theta$  is the local advection of the temperature field and  $LP - R$  is the enthalpy change from moist-thermodynamic processes. The strengths of the different terms again provide information about the transfers between different energetic components during the flow evolution. Enthalpy changes are driven by radiative relaxation, and in evaporating regimes the enthalpy increases as additional precipitating moisture is added. The decomposed enstrophy production components,  $\{\mathcal{Z}_t^{\text{Adv}}, \mathcal{Z}_t^{\text{Precip}}, \mathcal{Z}_t^{\text{Rad}}\}$ , are plotted in Figure 12 for cases with and without wind-induced evaporation, where  $\mathcal{Z}_t^{\text{Adv}}$  has been calculated as a residual.

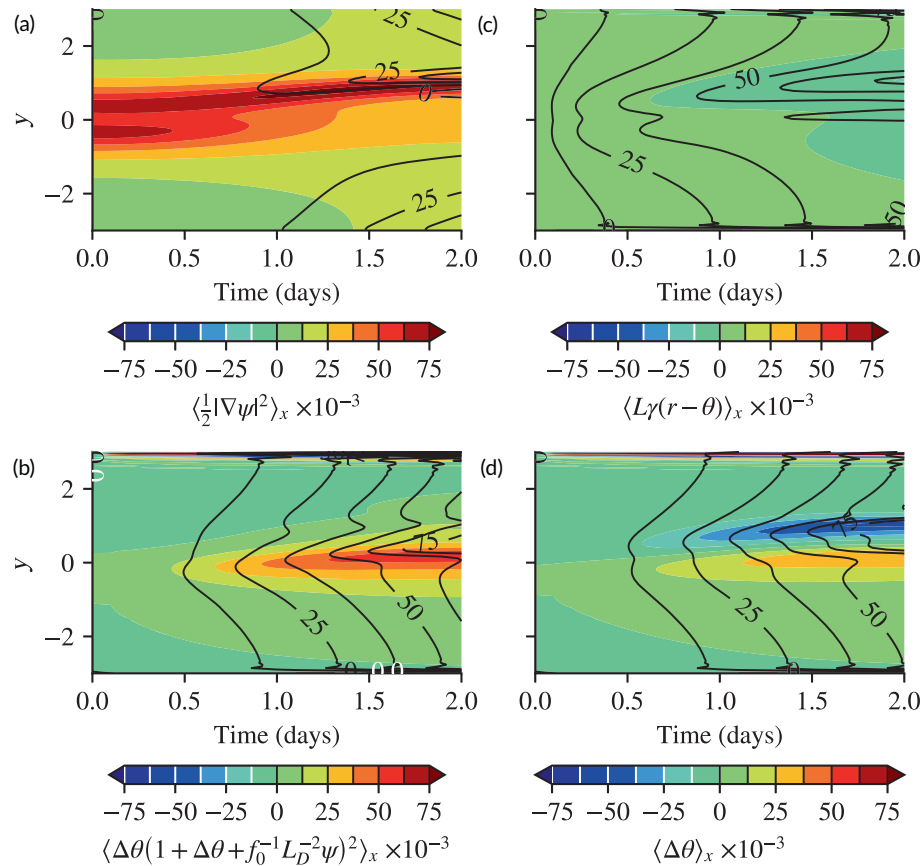


**FIGURE 11** Zonal-average energetic quantities in a numerical experiment of a large-amplitude perturbation on a  $\theta_y^e = 0.5$  background gradient. Shading shows the value without wind-induced evaporation, and contours indicate the additional anomaly with wind-induced evaporation ( $S^E = 0.1$ ). The quantities plotted are (a) kinetic energy density, (b) available potential energy due to the layer-thickness, (c) latent heating of condensation, and (d) thermal anomaly. Radiative heating of areas of dynamically driven negative thermal anomaly contribute to kinetic energy. Wind-induced evaporation contributes across these energetic quantities, centred on the vortex latitude. [Colour figure can be viewed at [wileyonlinelibrary.com](http://wileyonlinelibrary.com)]

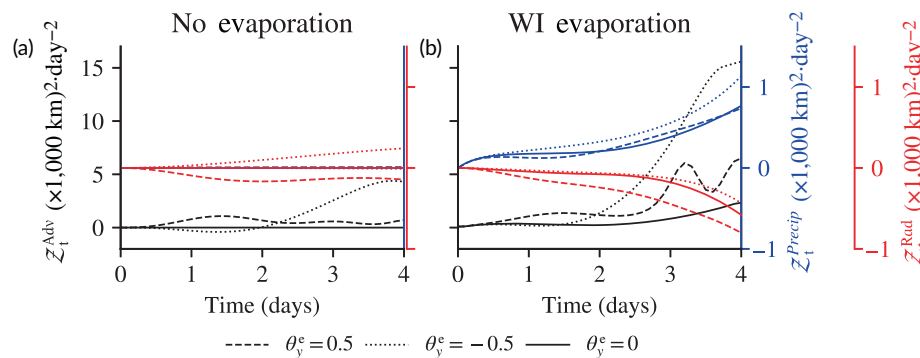


**FIGURE 12** Contributions to the rate of change of enstrophy in experiments with three background temperature gradients (see legend) and (a) without evaporation and (b) with wind-induced (WI) evaporation. [Colour figure can be viewed at [wileyonlinelibrary.com](http://wileyonlinelibrary.com)]

Without evaporation, where  $\theta_y^e \neq 0$  there is an diabatic increase in enstrophy through the condensation of water. With wind-induced evaporation, the enstrophy growth due to precipitation outpaces the diabatic cooling where  $\theta > \theta^e$ . The residual term describes how enstrophy is generated through the coupling of the flow with temperature gradients; there are periodic interference patterns due to cross-domain propagation of fast Rossby waves, and these are fastest for more positive  $\theta_y^e$ .

The production of enstrophy is dominated by  $Z_t^{\text{Adv}}$ , reflecting the contribution due to the adiabatic extraction of energy from the background state. Depending on the  $\theta_y^e$  background state,  $Z_t^{\text{Rad}}$  may be a source or sink of enstrophy through diabatic transfers. Without wind-induced evaporation (see Figure 12a), diabatic processes are driven

by radiative relaxation, with  $r \lesssim \theta$  due to the fast relaxation of excess moisture. With wind-induced evaporation (see Figure 12b), substantial precipitation rates are achieved that diabatically contribute enstrophy faster than the sink due to radiative relaxation. On the other hand, the increase in  $Z_t^{\text{Adv}}$  is much larger than that without wind-induced evaporation, amplifying directly in response to the interaction of higher wind speeds with anomalous temperature generation.

Figure 13 shows the accumulation over time of enstrophy in the system in the presence of wind-induced evaporation. The enstrophy amplification due to wind-induced evaporation is well approximated by an exponential function and is, therefore, proportional to the enstrophy itself. Following a spin-up period of approximately



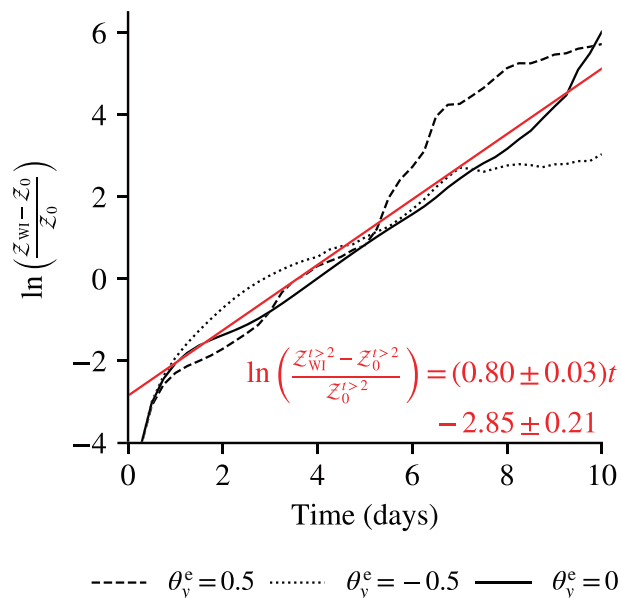


**FIGURE 13** Logarithm of normalised anomalous enstrophy versus time for 10-day integrations with wind-induced evaporation ( $S^E = 0.1$ ) and three background temperature gradients ( $\theta_y^e \in \{-0.5, 0, 0.5\}/(1000 \text{ km})$ ). The red line is a linear least-squares fit to the  $\theta_y^e = 0$  data (excluding days 1 and 2). The wind-induced anomalous growth in enstrophy is approximately exponential, with an e-folding time-scale of  $1/(0.80 \pm 0.03)$  days. [Colour figure can be viewed at [wileyonlinelibrary.com](http://wileyonlinelibrary.com)]

2 days, large-amplitude perturbations in experiments with negative, neutral, and positive background temperature gradients ( $\theta_y^e = -0.5, 0, 0.5$ ) all demonstrate a similar exponential growth in enstrophy, with an e-folding time-scale of  $\tau_{wl} = 1.25 \pm 0.05$  days. This time-scale decreases for an increased coefficient of wind-induced evaporation (not shown). Though in reality friction would curtail this growth, friction is not included in the model. The reader should note that hyperdiffusion in our model is set to be as weak as possible for the model to run for the length of these experiments and affects small-scale vorticity gradients, so has negligible effect on the large-scale organisation that enstrophy measures. The results shown in Figure 13 highlight the importance, in this idealised set-up, of wind-induced evaporation for energising large-amplitude perturbations. These results correspond with observations that the potential evaporation rate limits the genesis of South Asian MDs (Karmakar et al., 2021), which have a stratiform precipitation structure characteristic of maritime storms (Houze et al., 2011).

## 6 | SENSITIVITY TO THE BACKGROUND STATE

In this section, motivated by the changing climate (e.g., Arias et al., 2021), we used our idealised model to explore

the sensitivity of propagation of MD-like perturbations to different background conditions. We compare the propagation of large-amplitude perturbations in 4-day numerical experiments over a range of  $\theta_y^e \in [-1.5, 1.5]$  in 0.1 intervals. Zonal and meridional components of the propagation velocity are computed by tracking the vortex centre as the local minimum in  $\psi$  at times when a coherent vortex exists—see streamfunction tracking of observed depressions in Vishnu et al. (2020). The zonal and meridional propagation speeds,  $u_{\text{vortex}}$  and  $v_{\text{vortex}}$  respectively, are plotted in Figure 14a, alongside the heading calculated using these speeds (Figure 14b).

There is a clear dependence of propagation heading on the background temperature gradient (Figure 14a,b). For  $\theta_y^e < -1$  there is a strong sensitivity to  $\theta_y^e$ , and in particular a sharp westward change in heading with increasing temperature gradient. For  $\theta_y^e > 0$  and encompassing a summer-like  $\theta_y^e = 0.5$  background state, heading varies linearly with a sensitivity  $-24.4 \pm 1.4^\circ$  per unit change in  $\theta_y^e$ . For higher positive values of  $\theta_y^e$  there is a regime of fast westward propagation, with heading approaching due west (not shown). However, those experiments have only a short period before the initial vortex loses coherence due to interference with the periodic domain.

For experiments with wind-induced evaporation, there is a weaker sensitivity of propagation heading around  $\theta_y^e = 0$  (Figure 15a). We attribute this effect to a shielding of the vortex from the background gradient by a strong thermal anomaly driven by precipitation associated with wind-induced evaporation by the fast winds around the vortex centre. In this regime, the highest wind speeds are associated with the greatest shielding by the thermal anomaly. This reduces the sensitivity of propagation to changes in  $\theta_y^e$  in this intermediate regime (Figure 15b).

In these idealised experiments there is a quantifiable sensitivity of vortex propagation to the background state. In particular, we have focused on a background temperature gradient  $\theta_y^e$ , which tends to favour more westward propagation for more positive  $\theta_y^e$ . Around  $\theta_y^e = 0$  the propagation of the vortex is broadly consistent with beta-drift. However, for large positive  $\theta_y^e$ , the propagation is better understood as being dominated by thermal-Rossby waves that, consistent with the linear-stability analysis in Section 4, do not effectively organise precipitation. As a result, these fast westward-propagating modes are more weakly affected by wind-induced evaporation.

## 7 | SUMMARY

We have described a novel formulation by which moist dynamics are incorporated into a single-layer thermal

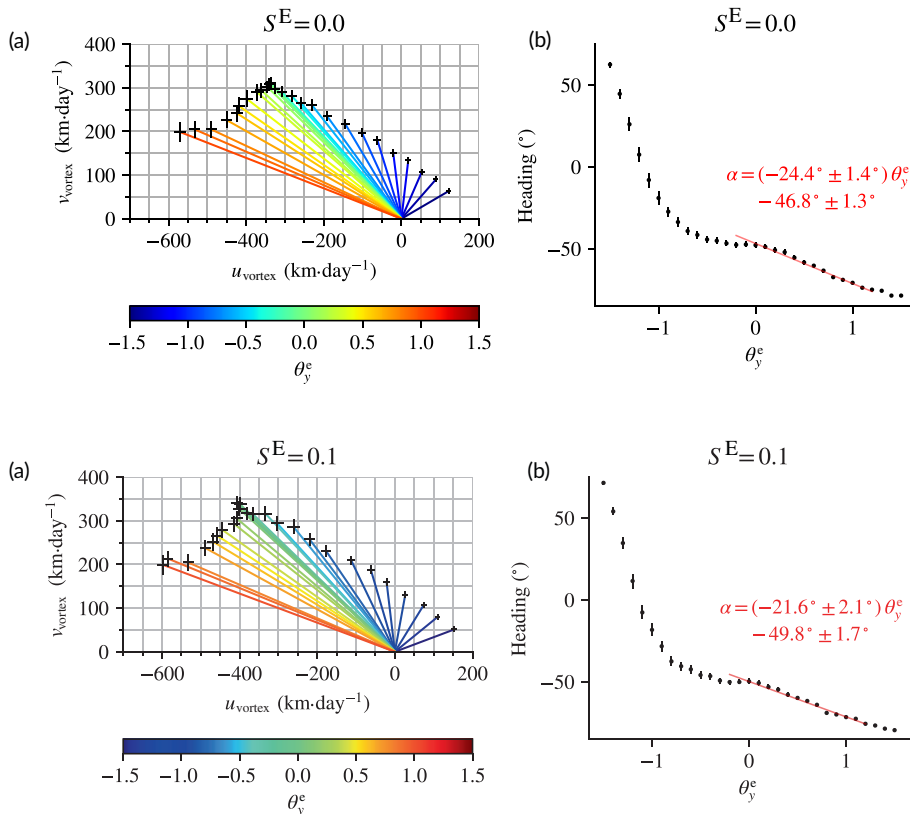


**FIGURE 14** (a) Meridional versus zonal components of the propagation velocity of the vortex centre—that is, the location of  $\min(\psi)$ —where a coherent vortex exists, for large-amplitude perturbation experiments, without wind-induced evaporation, across a range of background temperature gradients ( $\theta_y^e \in [-1.5, 1.5]$ ) (colours). Velocity components are estimated as linear fits of the  $x$ - and  $y$ -coordinates of the vortex centre versus time. (b) Vortex propagation heading for each experiment shown in (a), where heading is defined as the angular anomaly relative to pure northward propagation. For example, a northeastward-propagating vortex has a heading of  $45^\circ$  and a northwestward-propagating vortex has a heading of  $-45^\circ$ . For the intermediate regime,  $\theta_y^e \in [-0.1, 1.1]$ , a linear fit with inverse variance weighting (red line) highlights the sensitivity of propagation heading to the background temperature gradient. [Colour figure can be viewed at [wileyonlinelibrary.com](http://wileyonlinelibrary.com)]

**FIGURE 15** As Figure 14, except for experiments with wind-induced evaporation. [Colour figure can be viewed at [wileyonlinelibrary.com](http://wileyonlinelibrary.com)]

quasi-geostrophic model, with distinct PV, temperature, and specific humidity fields. The strengths of the moist-thermodynamic parameters have been scaled based on known time-scales of the processes they aim to reproduce, and background states have been set based on linear approximations of atmospheric reanalysis data in the South Asian monsoon region. The idealised model constitutes a relatively simple and interpretable tool for investigating prototype MDs.

A linear analysis of our model reveals a set of distinct modes that describe fast-propagating thermal-Rossby modes and stationary, amplifying, precipitating modes. These precipitating modes are shown to organise into

small-amplitude perturbations according to the sign of the background specific humidity gradient and the time-scale of excess moisture relaxation. The linearised model also demonstrates how the presence of a background precipitation gradient amplifies small-amplitude thermal-Rossby modes by coupling the dynamics to latent heating.

Numerical experiments further demonstrate how background conditions influence the dynamics of large-amplitude, MD-like disturbances. Using these experiments with nonlinear dynamics, we demonstrate the pathways of diabatic and adiabatic energy transfer into the disturbances and how these pathways are modified by a wind-induced evaporation feedback. In addition, a

series of numerical experiments testing the sensitivity of propagation to a range of background conditions shows a clear sensitivity of heading (i.e., propagation direction) to the imposed meridional temperature gradient. In particular, positive temperature gradients favour more westward propagation and negative gradients favour more eastward propagation. The model is consistent with the observations showing that MDs, which are characterised by strong westward propagation, occur only during the summer phase of the monsoon, when the meridional temperature gradient is positive. In contrast, the presence of negative meridional temperature gradients—corresponding with non-summer months in South Asia—inhibits westward propagation of MDs according to our model.

The inclusion of wind-induced evaporation in the model amplifies the rate of transfer of diabatic energy into kinetic energy and modifies the moisture structure of propagating disturbances. We further show that without wind-induced evaporation the model allows disturbances to derive energy through advective reorganisation of temperature to a state away from radiative equilibrium. The inclusion of wind-induced evaporation also increases the total enstrophy of disturbances through diabatic heating of condensing excess water, a process that is faster than diabatic cooling due to radiative relaxation. Therefore, a key finding is that wind-induced evaporation is an important mechanism for intensification in our model, which may offer some explanation for why deep MDs preferentially form over ocean (Karmakar et al., 2021), where we expect stronger surface evaporation feedbacks. For experiments with wind-induced evaporation on weak background temperature gradients, a shielding effect due to local diabatic heating counters the sensitivity of propagation to the background state. In this regime, beta-drift provides a good explanation for the propagation path. Such mechanisms based on nonlinear horizontal advection may provide a credible description of the large-scale dynamics of MDs, consistent with Boos et al. (2015).

Our model is highly idealised yet provides a simple conceptual framework for exploring the dynamics of MD-like disturbances and for testing their sensitivities to a range of climate states and parameters. A comparison between our idealised model and MDs simulated across a hierarchy of more comprehensive models is a priority for future work and would help to further fundamental understanding of these high-impact weather events in a changing climate.

#### FUNDING INFORMATION

AKC is supported by a St Leonard's College Interdisciplinary Doctoral Scholarship awarded by the University of St Andrews.

#### DATA AVAILABILITY STATEMENT

Data available on request from the authors.

#### ORCID

A. K. Chaudhri  <https://orcid.org/0000-0002-6716-1533>

M. P. Byrne  <https://orcid.org/0000-0001-9019-3915>

R. K. Scott  <https://orcid.org/0000-0001-5624-5128>

#### REFERENCES

- Adames, A.F. (2021) Interactions between water vapor, potential vorticity, and vertical wind shear in quasi-geostrophic motions: implications for rotational tropical motion systems. *Journal of the Atmospheric Sciences*, 78, 903–923 <https://journals.ametsoc.org/view/journals/atcsc/78/3/JAS-D-20-0205.1.xml>
- Adames, A.F. & Ming, Y. (2018a) Interactions between water vapor and potential vorticity in synoptic-scale monsoonal disturbances: moisture vortex instability. *Journal of the Atmospheric Sciences*, 75, 2083–2106.
- Adames, A.F. & Ming, Y. (2018b) Moisture and moist static energy budgets of south Asian monsoon low pressure systems in GFDL AM4.0. *Journal of the Atmospheric Sciences*, 75, 2107–2123.
- Arias, P., Bellouin, N., Coppola, E., Jones, R., Krinner, G., Marotzke, J. et al. (2021) *Technical summary*. Cambridge, UK: Cambridge University Press, pp. 33–144.
- Boos, W.R., Hurley, J.V. & Murthy, V.S. (2015) Adiabatic westward drift of Indian monsoon depressions. *Quarterly Journal of the Royal Meteorological Society*, 141, 1035–1048.
- Charney, J. (1955) The use of the primitive equations of motion in numerical prediction. *Tellus*, 7, 22–26 <https://onlinelibrary.wiley.com/doi/abs/10.1111/j.2153-3490.1955.tb01138.x>
- Chen, T.-C., Yoon, J.-H. & Wang, S.-Y. (2005) Westward propagation of the Indian monsoon depression. *Tellus A: Dynamic Meteorology and Oceanography*, 57, 758–769.
- Clark, S.K., Ming, Y. & Adames, A.F. (2020) Monsoon low pressure system-like variability in an idealized moist model. *Journal of Climate*, 33, 2051–2074.
- Cohen, N.Y. & Boos, W.R. (2014) Has the number of Indian summer monsoon depressions decreased over the last 30 years? *Geophysical Research Letters*, 41, 7846–7853.
- Cohen, N.Y. & Boos, W.R. (2016) Perspectives on moist baroclinic instability: implications for the growth of monsoon depressions. *Journal of the Atmospheric Sciences*, 73, 1767–1788.
- Cronin, T.W. & Emanuel, K.A. (2013) The climate time scale in the approach to radiative-convective equilibrium. *Journal of Advances in Modeling Earth Systems*, 5, 843–849.
- Diaz, M. & Boos, W.R. (2019a) Barotropic growth of monsoon depressions. *Quarterly Journal of the Royal Meteorological Society*, 145, 824–844.
- Diaz, M. & Boos, W.R. (2019b) Monsoon depression amplification by moist barotropic instability in a vertically sheared environment. *Quarterly Journal of the Royal Meteorological Society*, 145, 2666–2684.
- Goswami, B.N. (1987) A mechanism for the west-north-west movement of monsoon depressions. *Nature*, 326, 376–378.
- Hersbach, H., Bell, B., Berrisford, P., Hirahara, S., Horányi, A., Muñoz-Sabater, J. et al. (2020) The ERA5 global reanalysis. *Quarterly Journal of the Royal Meteorological Society*, 146, 1999–2049. Available from: <https://doi.org/10.1002/qj.3803>

- Houze, R.A., Rasmussen, K.L., Medina, S., Brodzik, S.R. & Romatschke, U. (2011) Anomalous atmospheric events leading to the summer 2010 floods in Pakistan. *Bulletin of the American Meteorological Society*, 92, 291–298.
- Hunt, K.M., Turner, A.G., Inness, P.M., Parker, D.E. & Levine, R.C. (2016) On the structure and dynamics of Indian monsoon depressions. *Monthly Weather Review*, 144, 3391–3416.
- Hurley, J.V. & Boos, W.R. (2015) A global climatology of monsoon low-pressure systems. *Quarterly Journal of the Royal Meteorological Society*, 141, 1049–1064.
- Karmakar, N., Boos, W.R. & Misra, V. (2021) Influence of intraseasonal variability on the development of monsoon depressions. *Geophysical Research Letters*, 48, e2020GL090425 <https://agupubs.onlinelibrary.wiley.com/doi/abs/10.1029/2020GL090425>
- Kitoh, A., Endo, H., Krishna Kumar, K., Cavalcanti, I.F., Goswami, P. & Zhou, T. (2013) Monsoons in a changing world: a regional perspective in a global context. *Journal of Geophysical Research Atmospheres*, 118, 3053–3065.
- Krishnakumar, V., Keshavamurty, R.N. & Kasture, S.V. (1992) Moist baroclinic instability and the growth of monsoon depressions—linear and nonlinear studies. *Proceedings of the Indian Academy of Sciences - Earth and Planetary Sciences*, 101, 123–152.
- Krishnamurti, T.N., Martin, A., Krishnamurti, R., Simon, A., Thomas, A. & Kumar, V. (2013) Impacts of enhanced CCN on the organization of convection and recent reduced counts of monsoon depressions. *Climate Dynamics*, 41, 117–134.
- Krishnamurti, T.N., Molinari, J., Pan, H. & Wong, V. (1977) Downstream amplification and formation of monsoon disturbances. *Monthly Weather Review*, 105, 1281–1297.
- Kurganov, A., Liu, Y. & Zeitlin, V. (2020) Moist-convective thermal rotating shallow water model. *Physics of Fluids*, 32, 066601. Available from: <https://doi.org/10.1063/5.0007757>
- Kurganov, A., Liu, Y. & Zeitlin, V. (2021) Interaction of tropical cyclone-like vortices with sea-surface temperature anomalies and topography in a simple shallow-water atmospheric model. *Physics of Fluids*, 33, 106606.
- Lam, J.S.-L. & Dritschel, D.G. (2001) On the beta-drift of an initially circular vortex patch. *Journal of Fluid Mechanics*, 436, 107–129.
- Lindzen, R.S., Farrell, B. & Rosenthal, A. (1983) Absolute barotropic instability and monsoon depressions. *Journal of the Atmospheric Sciences*, 40, 1178–1184 [https://journals.ametsoc.org/view/journals/atsc/40/5/1520-0469\\_1983\\_040\\_1178\\_abiamd\\_2\\_0\\_co\\_2.xml](https://journals.ametsoc.org/view/journals/atsc/40/5/1520-0469_1983_040_1178_abiamd_2_0_co_2.xml)
- Mohebalhojeh, A.R. & Dritschel, D.G. (2001) Hierarchies of balance conditions for the f-plane shallow-water equations. *Journal of the Atmospheric Sciences*, 58, 2411–2426.
- Monteiro, J.M. & Sukhatme, J. (2016) Quasi-geostrophic dynamics in the presence of moisture gradients. *Quarterly Journal of the Royal Meteorological Society*, 142, 187–195.
- Penman, H.L. & Keen, B.A. (1948) Natural evaporation from open water, bare soil and grass. *Proceedings of the Royal Society of London. Series A. Mathematical and Physical Sciences*, 193, 120–145 <https://royalsocietypublishing.org/doi/abs/10.1098/rspa.1948.0037>
- Rao, K. & Rajamani, S. (1970) Diagnostic study of a monsoon depression by geostrophic baroclinic model. *Indian Journal of Meteorology & Geophysics*, 21, 187–194.
- Rastogi, D., Ashfaq, M., Leung, L.R., Ghosh, S., Saha, A., Hodges, K. et al. (2018) Characteristics of bay of Bengal monsoon depressions in the 21st century. *Geophysical Research Letters*, 45, 6637–6645.
- Rostami, M. & Zeitlin, V. (2022) Instabilities of low-latitude easterly jets in the presence of moist convection and topography and related cyclogenesis, in a simple atmospheric model. *Geophysical and Astrophysical Fluid Dynamics*, 116, 56–77. Available from: <https://doi.org/10.1080/03091929.2021.1959574>
- Shukla, J. (1977) Barotropic-baroclinic instability of mean zonal wind during summer monsoon. *Pure and Applied Geophysics*, 115, 1449–1461.
- Sobel, A.H. & Bretherton, C.S. (2000) Modeling tropical precipitation in a single column. *Journal of Climate*, 13, 4378–4392.
- Suhas, D.L. & Boos, W.R. (2023) Monsoon depression amplification by horizontal shear and humidity gradients: a shallow water perspective. *Journal of the Atmospheric Sciences*, 80, 633–647 <https://journals.ametsoc.org/view/journals/atsc/80/2/JAS-D-22-0146.1.xml>
- Tompkins, A.M. & Craig, G.C. (1998) Time-scales of adjustments to radiative-convective equilibrium in the tropical atmosphere. *Quarterly Journal of the Royal Meteorological Society*, 124, 2693–2713.
- Vishnu, S., Boos, W.R., Ullrich, P.A. & O'Brien, T.A. (2020) Assessing historical variability of south Asian monsoon lows and depressions with an optimized tracking algorithm. *Journal of Geophysical Research: Atmospheres*, 125, e2020JD032977.
- Vishnu, S., Francis, P.A., Shenoi, S.C. & Ramakrishna, S.S. (2018) On the relationship between the Pacific decadal oscillation and monsoon depressions over the bay of Bengal. *Atmospheric Science Letters*, 19, 1–8.
- Warneford, E.S. & Dellar, P.J. (2013) The quasi-geostrophic theory of the thermal shallow water equations. *Journal of Fluid Mechanics*, 723, 374–403.
- Zerroukat, M. & Allen, T. (2015) A moist Boussinesq shallow water equations set for testing atmospheric models. *Journal of Computational Physics*, 290, 55–72. Available from: <https://doi.org/10.1016/j.jcp.2015.02.011>
- Zhang, Y. & Fueglistaler, S. (2020) How tropical convection couples high moist static energy over land and ocean. *Geophysical Research Letters*, 47, 1–8.
- Zhao, B., Zeitlin, V. & Fedorov, A.V. (2021) Equatorial modons in dry and moist-convective shallow-water systems on a rotating sphere. *Journal of Fluid Mechanics*, 916, 1–33.

**How to cite this article:** Chaudhri, A.K., Byrne, M.P. & Scott, R.K. (2024) A moist-thermal quasi-geostrophic model for monsoon depressions. *Quarterly Journal of the Royal Meteorological Society*, 1–20. Available from: <https://doi.org/10.1002/qj.4723>